CrossMark

J. Fluid Mech. (2022), *vol*. 952, A29, doi:10.1017/jfm.2022.910

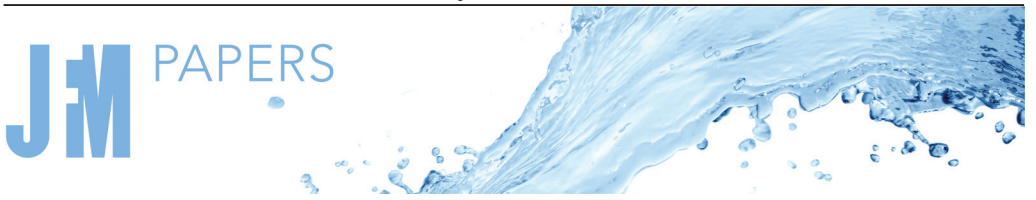

Hydrodynamic cavitation reduction in semidilute turbulent polymer solution flows

Reza Azadi[1] **and David S. Nobes**[1],†

[1]Department of Mechanical Engineering, University of Alberta, Edmonton, Alberta T6G1H9, Canada

(Received 10 June 2022; revised 22 September 2022; accepted 25 October 2022)

The hydrodynamic cavitation in semidilute solution flows of a flexible polymer additive in water was experimentally explored in a mesoscale converging–diverging nozzle to elucidate the cavitation reduction effects of polymer additives. Rheological measurements demonstrated that polymer solutions were shear-thinning, with infinite viscosities larger than pure water. The polymer additives significantly mitigated the intensity of cloud cavitation and the growth of violent cavity structures in the tested solution concentrations. Under conditions of supercavitation, the tested polymer solutions could not suppress the growth of large structures but showed a reduction in the population of cavitation bubbles. The temporal evolution and spatial variation of cavitation structures in different concentrations were captured using high-speed imaging. Statistical analysis of the images showed that polymers reduce cavitation via three main mechanisms. (1) The longitudinal expansion of cavities downstream is attenuated relative to the pure water. The streamwise distribution of vapour-ratio fluctuations was flattened, and its peak was shifted upstream in the solutions. (2) Mean collapse and growth rate of cavitating bubble pockets and their fluctuations were noticeably relaxed by polymer additives. For a 400 p.p.m. solution (parts per million (p.p.m.)), a reduction of 65 % was measured relative to pure water flow at the highest tested flow rate. (3) Spectral analysis of the downstream pressure indicated that the shedding frequency at the cavitation inception was reduced as the solution's concentration increased. This reduction was as high as 70 % for a 400 p.p.m. solution. These results highlight the strong interplay between polymer additives and the generation of cavitation-related structures.

Key words: cavitation, drag reduction, viscoelasticity

1. Introduction

Flow parameters such as pressure and velocity can show relatively high fluctuation levels in a turbulent flow regime. Under certain circumstances, instantaneous pressure at

† Email address for correspondence: david.nobes@ualberta.ca

© The Author(s), 2022. Published by Cambridge University Press. This is an Open Access article, distributed under the terms of the Creative Commons Attribution licence (https://creativecommons.org/licenses/by/4.0/), which permits unrestricted re-use, distribution, and reproduction in any medium, provided the original work is properly cited.

https://doi.org/10.1017/jfm.2022.910 Published online by Cambridge University Press

any point of a wall-bounded turbulent flow, $p(\boldsymbol{x}, t)$, can experience a drop well below the fluid's saturation pressure p_{sat} at a specified temperature T_L, i.e. the condition of $p(\boldsymbol{x}, t) \ll p_{sat}(T_L)$. As a result, a local phase change occurs, and microscale vapour (or cavitation) bubbles emerge in the bulk liquid flow. This phenomenon triggers the onset of the cavitation process and is commonly called the cavitation inception regime (Rood 1991). An instant later, the local pressure may recover to a value higher than p_{sat}, which causes the cavitation bubbles to collapse in microseconds (Brennen 2013). Simultaneous growth and collapse of the cavitation bubbles at different regions of the flow field are intrinsic characteristics of the cavitation phenomenon, and one cannot exist without the other. The higher the pressure fluctuations relative to p_{sat}, the more violent the spatial growth and collapse of the vapour bubbles, resulting in the agglomeration of tiny bubbles and the generation of large-scale cavitation clouds (Arndt 2002).

The sudden collapse of microbubbles is followed by an extreme increase in local pressures up to 85 MPa and temperatures up to 6400 °C at the bubble centroid (Fujikawa & Akamatsu 1980). Extreme pressure gradients in the vicinity of the collapsing bubbles generate local liquid microjets with relatively high momentum. Zeng, Gonzalez-Avila & Ohl (2020) investigated the dynamics of such jets in a thin liquid layer confined between two rigid walls and showed that these liquid jets could gain impact speeds up to 200 m s^{-1}. The collapse generates relatively high-momentum shockwaves, which mostly propagate upstream of the flow and modify the dynamics of the incoming liquid flow (Ganesh, Mäkiharju & Ceccio 2016). The complex interaction of growing and collapsing bubble pockets with the bulk turbulent flow and the wall boundaries, accompanied by the propagating shockwaves, results in different cavitation regimes, which can be qualitatively grouped as inception, sheet, cloud, developing and supercavitation regimes (Brennen 2013).

An acoustic or ultrasound field (Curtiss *et al.* 2013; Murakami *et al.* 2021) applied to a flow, or sudden acceleration and deceleration of the flow can cause $p(\boldsymbol{x}, t)$ to fluctuate around $p_{sat}(T_L)$ and trigger the cavitation process. In some applications, conditions for cavitation to occur are intentionally created. For instance, microsized bubbles can be manipulated to carry antibiotics and cancer-treatment drugs to malignant tissues, where ultrasound fields are externally applied to collapse the bubbles and release the therapeutic drugs *in vitro* (Stride & Coussios 2019; Versluis *et al.* 2020). The generated shockwaves and microjets locally penetrate the cancerous tissues and open a path for the drug molecules to dive into deeper levels of the tissues, which significantly enhances the efficacy of the drug delivery process (Stride *et al.* 2020).

The collapse of bubbles near solid walls generates relatively high shear stress regions and high moment re-entrant liquid jets adjacent to the fast deforming bubbles where the combined effect is utilized in removing dirt and cleaning surfaces (Chahine *et al.* 2016; Verhaagen & Fernández Rivas 2016). Turner *et al.* (2019) explored the exfoliation of graphene layers using ultrasonication and showed that control and optimization of the acoustic cavitation results in higher rates of exfoliated graphene at shorter sonication periods. Cavitation is also advantageous in destroying microorganisms (Zupanc *et al.* 2019) and disinfecting water (Mane *et al.* 2020). Using a hydrodynamic cavitation process, where a low concentration of peppermint oil was added to the flow, Mane *et al.* (2020) showed that a disinfection rate of more than 99 % could be achieved in relatively short times.

In contrast to the scenarios where cavitation can be advantageous, cavitation can cause noise, vibration, erosion and noticeable damage to equipment in most industrial applications. Dular *et al.* (2004) used three different hydrofoil configurations covered with copper foil to examine the impact of hydrodynamic cavitation on surface erosion.

https://doi.org/10.1017/jfm.2022.910 Published online by Cambridge University Press

Using image processing, they detected and counted the number of pits produced on the copper surfaces that had undergone violent cavitation and correlated this to cavitation structures they had visualized. In an experimental study on a converging–diverging venturi channel, Xu *et al.* (2020) showed that the noise level strongly depended on the outlet to inlet pressure ratio, $p_r = p_{out}/p_{in}$, and had a peak at $p_r \approx 0.9$.

Any alteration of the wall geometry, thermophysical properties of the fluid, or body forces being applied to the flow field that can avoid or delay the local pressure drop below its saturation pressure, can reduce cavitation intensity. In the past years, researchers used various passive and active methods to control the inception or intensity of cavitation. Chatterjee & Arakeri (1997) generated synthetic cavitation at the throat of a converging–diverging venturi by injecting electrolysis bubbles at the channel's inlet to act as free stream nuclei. They applied an acoustic pressure field upstream of the throat using a ring piezoelectric transducer and showed that cavitation was noticeably suppressed at the throat. In their experiments, the synthetic bubbles experienced sudden cavitation and collapsed as they passed the acoustic field and disintegrated into dissolved nuclei in the bulk liquid, mitigating the potential of cavitation inception at the throat.

Kawanami *et al.* (1997) investigated the feasibility of passively controlling the generation of cloud cavitation on a hydrofoil using small square obstacles attached to the hydrofoil surface. They used straight acrylic obstacles with square cross-sections and tested different configurations relative to the streamwise flow direction. Their results showed that when the obstacle covered the entire spanwise width of the hydrofoil and was positioned at ≈37 % of the chord length relative to the leading edge of the hydrofoil, peak pressure fluctuations were damped out by 40 %, and the noise level was reduced by 5–20 dB, indicating that cloud cavitation was suppressed. In a cloud cavitation regime with no obstacles, a continuous layer of re-entrant liquid flows upstream on the wall surface towards the throat, where it cuts off the growing sheet cavities and elevates the cloud cavitation process. The addition of an obstacle at this position breaks the chain of events for the cloud cavitation to maintain. The re-entrant flow stagnates at the obstacle and loses its momentum, and only small-scale cavity structures are generated at the closure of the sheet cavities.

Following the first study by Toms (1948), it has been well understood in recent years that the addition of minute amounts, in orders of parts per million (p.p.m.), of long-chain polymers to a turbulent liquid flow has significant drag-reducing (DR) effects (White & Mungal 2008; Xi 2019), which can be as high as 60 % in a pipe flow (Owolabi, Dennis & Poole 2017). As the polymer solution flow experiences continuous shear stress, such as during the circulation of a fluid in a closed-loop system, the DR effects decay due to the scission of polymer molecules, a phenomenon commonly known as the mechanical degradation of the polymers (den Toonder *et al.* 1995). Stretch of long-chain polymers with relaxation times larger than the turbulent time scale thickens the buffer layer and modifies the mean velocity profile, resulting in a different distribution of wall shear stresses (White & Mungal 2008; Warwaruk & Ghaemi 2021). Based on the elastic theory (Tabor & de Gennes 1986), elongated polymer molecules extract energy from the viscous sublayer and store it as elastic energy (Min *et al.* 2003). When the relaxation time is sufficiently long, the stored energy is transported and released into the buffer and log-law layers (Min *et al.* 2003). The released energy enhances the streamwise turbulence intensity and attenuates the fluctuations of the wall-normal and spanwise velocities, which results in a reduction in the wall shear stress and causes DR (Min *et al.* 2003; Ptasinski *et al.* 2003; Dubief *et al.* 2004; Arosemena, Andersson & Solsvik 2020).

Significant DR effects of polymer additives have also been of interest to researchers in the field of cavitating two-phase flows to explore the feasibility of cavitation

https://doi.org/10.1017/jfm.2022.910 Published online by Cambridge University Press

reduction (CR) effects of these additives. Brennen (1970) used a variety of bulk bodies, including spheres of different sizes, a cylinder and a disk, and exposed them to an incoming flow of different additive solutions. Dilute solutions of a surface tension reducing agent, three types of rigid and flexible polymers and a cationic surfactant were tested at different free stream velocities. It was shown that a dilute polymer solution did not have any practical effect on the cavity flow behind the disk. In contrast, the attached flow behind the spherical and cylindrical bodies was destabilized in the polymer solution and caused separation line distortion and cavitation interface irregularities.

Hoyt (1976) investigated the effect of polyethylene oxide (PEO) on the cavitation inception number σ_i of a cavitating jet flow. This number was defined as $\sigma_i = (p - p_v)/0.5\rho U^2$ in the experiments, where p was defined as the mean static pressure of the main stream, p_v was the saturation pressure of water at the test temperature, ρ was the density of the solution and U was denoted as the mean bulk fluid velocity. The results show that concentrations as low as 8 p.p.m., reduced σ_i by $\approx$40 % relative to the pure water flow. The viscosity and air content were measured to be similar in the water and PEO solution. Ting (1978) utilized different concentrations of PEO and polyacrylamide (PAM) solutions in water to study the effect of these additives on the cavitation mechanism on the surface of a rotating disk. Ting (1978) showed that σ_i was reduced $\approx$65 % in a 500 p.p.m. solution of PEO at the tested flow rate. The author argued that high deceleration rates adjacent to the stagnation point on the disk caused relatively high viscoelastic stresses that suppress the cavitation and reconfigure its topology. Ōba, Itō & Uranishi (1978) showed that in a flow through a circular orifice, desinence cavitation number σ_d decreases significantly for 10 p.p.m. PEO solution in water. Increasing the concentration to 50 p.p.m. proliferated the population of non-spherical cavitation bubbles, attenuated pressure fluctuations and shifted the dominant shedding frequency to lower values relative to the pure water flow. In an extensive review of the studies conducted before 1997, Fruman (1999) concluded that the polymers have consequential effects on the boundary layers developed on the solid bodies and the topology of large-scale vortices interacting with individual cavitating bubbles. It was argued that this complexity was the major obstacle to a comprehensive understanding of the phenomenon.

Hasegawa, Ushida & Narumi (2009) measured the pressure drop over different sizes of orifices, ranging from 5 to 400 µm, in submerged jet flows of pure water, 50 w w^{-1} mixture of water and glycerol and a 1000 p.p.m. PEO solution in water. For all the tested conditions, they showed relatively large reductions of pressure drop, except in the 400 µm orifice. The authors reported that the viscosity of the PEO solution was similar to water, i.e. $\approx$1 mPa s. Wall slip and elasticity of the PEO solutions were introduced as the main causes of pressure drop reductions. As discussed by Brujan (2011), dilute polymeric solutions mostly demonstrate shear-thinning behaviour, with dynamic viscosities relatively higher than pure water for low and intermediate shear strain rates. Hence, it is essential to measure detailed rheological characteristics of non-Newtonian solutions in an experiment to properly address the role of the fluid's elasticity in the obtained results.

Naseri *et al.* (2018) simulated the dynamics of cavitating turbulent Phan–Thien–Tanner (PTT) viscoelastic fluids in a step and an injector nozzle. They used the wall-adapting local eddy viscosity subgrid-scale turbulence model adapted for large eddy simulation to simulate the turbulent flow. The PTT and Schnerr and Sauer models were used to simulate the flow's viscoelasticity and cavitation, respectively. Their results showed that flow's viscoelasticity suppressed cavitation inside the stepped nozzle relative to the pure water flow. They argued that the main physical causes of the cavitation suppression were annihilation of cavitating microvortices in the shear layer and reduction in the

https://doi.org/10.1017/jfm.2022.910 Published online by Cambridge University Press

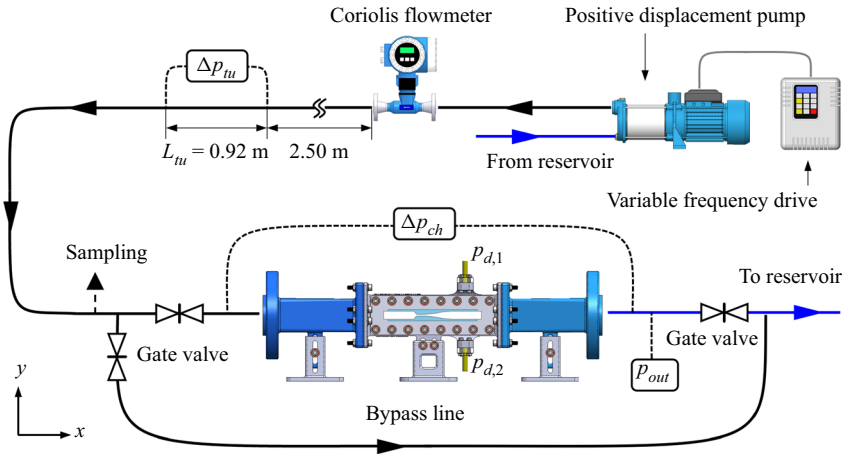

Figure 1. Schematic representation of the flow loop and its main components (not to scale).

turbulence intensity. They also reported that the viscoelastic suppression of turbulence inside the injector nozzle alleviated the generation of string cavitation structures.

The dynamics of the interaction of viscoelastic semidilute polymer solutions with microsized cavitation bubbles at the inception or with large-scale bubble pockets in a violent regime such as cloud cavitation are not well understood. It is unclear whether these additives can suppress or attenuate highly intense cavitation regimes such as supercavitation when their molecules can experience extreme extensional shears. This study aims to answer these questions by shedding light on the dynamics of the cavitation phenomenon in flowing semidilute polymer solutions in a wall-bounded converging–diverging mesoscale channel. Information obtained from high-speed imaging and pressure sensor data was analysed using various image processing and statistical techniques to elucidate the intricacies of this complex flow phenomenon.

2. Experimental system

2.1. *Flow facility*

A mesoscale flow loop was designed to examine the cavitation mechanism in a converging–diverging channel. A schematic of the experimental system is shown in figure 1. A positive displacement pump (Model 33204; Moyno Inc.), equipped with a variable frequency drive circulated the flow in the loop. The flow's mass flow rate, density, and temperature were measured online using a Coriolis flowmeter (Krohne Optimass 7000), which communicated with the computer via RS-485 Modbus protocol. A custom code based on the MODBUS interface of the instrument control toolbox of MATLAB (2021; MathWorks) was developed to read, control and store flowmeter signals. For each test, data was collected for 10 s.

As shown in figure 1, the flow system was designed as the channel section can be bypassed from the main loop by closing a gate valve at its inlet. This way, water–additive mixtures circulated in the system at moderate flow rates and for a certain period to generate a more homogeneous solution before undergoing the cavitation process within the channel. At each test, the liquid flow's pressure drop over the straight tube Δp_{tu} was measured over $L_{tu} = 0.92$ m in a circular, straight plastic tube with an inner diameter of $D_{tu} = 19$ mm. A differential pressure transducer (DP15; Validyne Engineering) with a

https://doi.org/10.1017/jfm.2022.910 Published online by Cambridge University Press

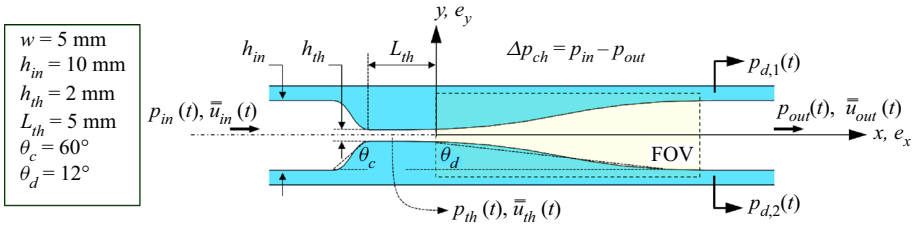

Figure 2. Schematic representation of the flow path and the main dimensions and flow variables. The interrogated field-of-view (FOV) is highlighted with a pale-yellow rectangle, with its boundaries shown by dashed lines. The origin of the coordinate system is vertically located on the channel's centreline and horizontally located at the start of the divergence region.

transducer diaphragm (no. 3-26; Validyne Engineering), calibrated for a full-scale (FS) pressure of 2.0 kPa, measured Δp_{tu} at a scan rate of 500 Hz.

As figure 1 illustrates, the flow was delivered to the test section via a contraction. The contraction smoothly transformed the circular cross-section of the flow path with a diameter of 26.7 mm into a rectangular entrance of 10 mm × 2 mm. A honeycomb was designed with uniformly distributed hexagonal hollows of inscribed circle diameter of 1.5 mm, with an edge-to-edge distance of 0.2 mm, to straighten the incoming flow. The honeycomb had a length of 15 mm, and its outer face followed the internal topology of the contraction section at 75 mm from the test section's entrance.

As illustrated in figure 2, the flow entered and exited the test section through a rectangular opening with a 10 mm × 5 mm ($h_{in} \times w$) cross-sectional area. The width of the flow path was kept constant over the test section at $w = 5$ mm. At 30.7 mm from the nozzle's starting edge, the channel's height decreases with a convergence angle of $\theta_c = 60^\circ$ over 5.2 mm. In the throat, height is constant, $h_{th} = 2$ mm, for a length of $L_{th} = 5$ mm. The channel's height increases smoothly again at a divergence angle of $\theta_d = 12^\circ$ over 42.3 mm and reaches a zero slope, 26.8 mm from the outlet. The wall profiles were generated based on a third-order polynomial profile, with their starting and ending points tangent to the horizontal flow path. Two transparent windows were laser cut from 1/4 in. acrylic sheet (Optix acrylic; Plaskolit Inc.) using a commercial laser cutter (VersaLaser V.L.D. Version 3.50; Universal Laser Systems) and were installed on both sides of the channel to give optical access to the interior flow. The flow left the test section via a diffuser section, identical to the contraction, and returned to the water reservoir with a capacity of ≈20 l.

The contraction and diffuser sections shown in figure 1, the honeycomb, the test section and the converging–diverging nozzles were constructed using the low force stereolithography technology (Form 3; Formlabs Inc.). The print resolution was 50 µm for the nozzles and 100 µm for all other parts. Transparent resin (V4; FormLabs Inc.) was used as the base material for printing the test section and the nozzles, and for the other printed components, grey resin (V4; FormLabs Inc.) was used. The nozzles can be easily separated from the test section and replaced with different nozzle shapes to generate different configurations, such as an asymmetric converging–diverging flow path. The nozzle surfaces were polished using ultrafine microgrit sandpapers. Finally, a plastic polish (7100 Plastic Polish Kit; NOVUS Plastic Polish) was used to remove microscratches on the surface. The final surface finish was sufficiently smooth and glossy.

Two differential pressure transducers (DP15; Validyne Engineering) measured the pressure drop Δp_{ch} over the test section and the outlet pressure p_{out} at a scanning frequency

https://doi.org/10.1017/jfm.2022.910 Published online by Cambridge University Press

of 500 Hz. The Δp_{ch} and p_{out} transducers used, respectively, diaphragm (no. 3-48; Validyne Engineering) calibrated for FS = 500 kPa, and diaphragm (no. 3-20; Validyne Engineering) calibrated for FS = 800 Pa. The accuracy of the pressure drop measurements was ±0.5 % FS. Pressure transducers were calibrated with a portable pressure calibrator (DPI 603; Druck, Baker Hughes business) based on 15 discrete measurements for a full-scale output voltage of 10 V and fitting a line to the time-averaged pressure data. The coefficient of determination of the fitted curves was ≈1. The output voltage signals were conditioned using a multichannel carrier demodulator (CD280; Validyne Engineering) with a maximum frequency response of 1 kHz. As shown in figure 1, to measure the dynamic pressure fluctuations of the flow, two high-frequency quartz pressure sensors (112A05, charge type; P.C.B. Piezotronics) were mounted in the downstream flow at the top and bottom of the test section. The sensitivities of the pressure sensors were 0.1749 pc $(\text{kPa})^{-1}$ and 0.1715 pc $(\text{kPa})^{-1}$ for $p_{d,1}$, and $p_{d,2}$. A signal conditioner (482C54; P.C.B. Piezotronics) with a charge sensitivity of 10 mV pc^{-1} was used to charge the sensors. Full-scale pressure measurement and output voltage were 100 kPa and 10 V, respectively. The gain values were adjusted for each sensor to give an output sensitivity of 100 mV $(\text{kPa})^{-1}$ for both sensors. The scanning frequency of the pressure sensors was 125 kHz. A voltage input module (NI-9205; National Instruments) installed on a compact data acquisition chassis (Ni-cDAQ-9188; National Instruments) read the incoming pressure signals and transferred them to the computer via an Ethernet connection. Two resistance temperature detectors (TR40; WIKA Instruments Canada Ltd.) measured the incoming and outgoing flow temperatures. A temperature input module installed on the same chassis read temperatures at 200 Hz. A custom code based on the data acquisition toolbox of MATLAB (2021; MathWorks) was developed to read and store pressure and temperature signals.

2.2. *Optical set-up*

As figure 3 shows, the flow field was interrogated using an optical system based on backlit illumination. A green-light high-current light-emitting diode (LED) (iLA.LPS v3; ILA 5150 GmbH) with a maximum frequency of 1 MHz illuminated the FOV. As illustrated in figure 3, two biconvex lenses and a diffuser were used in sequence in front of the LED. Their distances from the channel's central plane were carefully tuned to focus the light and distribute it uniformly on the FOV. A microcalibration glass target (MP 50 × 12; LaVision GmbH) was utilized to calibrate the images and focus on the midspan of the channel (plane $z = 0$). Dot targets with diameters of 100 ± 1 µm and equal planar distancing of 300 ± 1 µm of the target plane were found to be suitable for the calibration. Due to the geometrical constrictions of the test section, it was not feasible to put the calibration plate within the channel and adjust its position to calibrate the imaging system. Therefore, the apparent width of the test section was carefully measured, and the position of the channel's midspan relative to the channel's front window was determined with high certainty. The camera was focused on the dots of the target plate mounted on the channel's front window. Then, using a combination of a one-axis linear stage (M-460P-X; Newport Corporation) and a Vernier micrometre (SM-25; Newport Corporation), the camera was carefully moved in increments of 1 µm towards the front window at a distance equal to the apparent width of the midspan plane relative to the target's focal plane. This procedure allowed spatial calibration of the image at a known position and z location within the channel.

A high-speed camera (Phantom V611; Vision Research Inc.) recorded 17 000 images with a frame rate of 19 kHz ($\Delta t \approx 52.6$ µs) for each flow scenario. The camera and LED

https://doi.org/10.1017/jfm.2022.910 Published online by Cambridge University Press

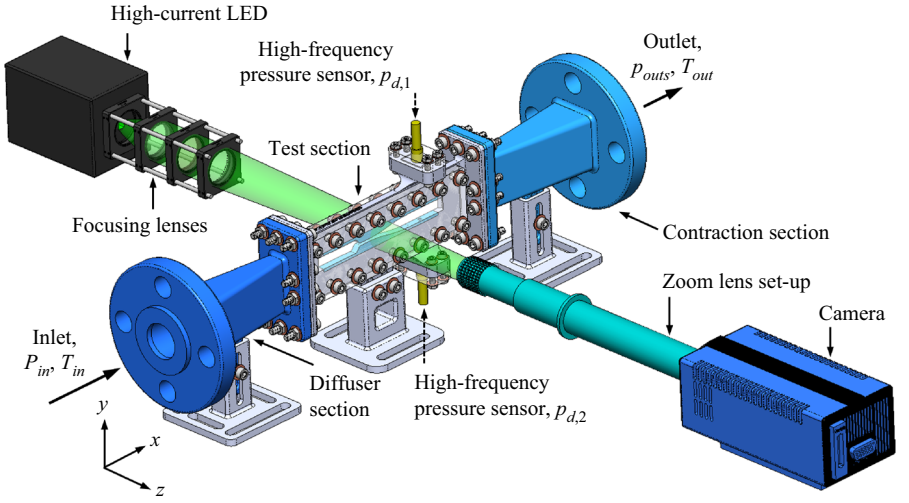

Figure 3. Backlit illuminated optical set-up to visualize the flow. The high-current LED was equipped with biconvex lenses to focus the light beams and a diffuser to distribute them uniformly in the region of interest.

e (μm)	f_c (kHz)	Δt_{exp} (ns)	R (pixel^2)	FOV (mm^2)	M	ξ (μm pixel^{-1})	δ_{of} (μm)
20	19	237	1008 × 320	26.2 × 8.3	0.77	25.92	893.66

Table 1. Main optical properties of the imaging system.

were carefully synchronized and triggered by adjusting the trigger signal's delay, period and duty using a function generator (AFG 3021B, Tektronix Inc.). The camera's exposure time and the LED's power were adjusted to saturate ≈80 % of the camera's sensors in the liquid region (equivalent to ≈204/255 image counts). The LED's duty duration was set to 237 ns (≈0.45 % of the full cycle) to freeze the fastest motion of cavitation structures. Table 1 lists the main optical properties of the imaging system. An average of 1000 images of ≈ 700 target dots was used in a third-order polynomial fit model to map the images to the real-world coordinates. The fit's root-mean-square (r.m.s.) was less than 0.1 for all cases. Commercial software (DaVis V8.2; LaVision GmbH) was used for the mapping process. A zoom lens (12X, 1-50486; Navitar Inc.) with an extension adapter (1X, 1-6015; Navitar) and a lens attachment (0.5X, 1-50012; Navitar Inc.) was used to obtain a magnification of $M \approx 0.77$ and digital resolution of $\xi \approx 25.92\,\mu\text{m pixel}^{-1}$. The formulation (Inoué & Spring 1997)

$$\delta_{of} = \frac{n_{RI}\lambda}{(N_A)^2} + \frac{n_{RI}e}{M\,(N_A)}, \tag{2.1}$$

was used to calculate the depth of field δ_{of} value. Here, $n_{RI} = 1$ is the refractive index of air, the medium between the lens and the object under study, $\lambda = 532$ nm is the wavelength of the green light, $e = 20\,\mu\text{m}$ is the discrete sensor size and $N_A = 0.043$ is the numerical aperture of the zoom lens system.

https://doi.org/10.1017/jfm.2022.910 Published online by Cambridge University Press

C_s (p.p.m.)	Pure water	50	100	200	400
$Re_{th} \times 10^{-4}$	2.3–5.4	2.1–5.3	2.1–5.2	2.2–5.1	2.1–4.8
$Re_{th,i} \times 10^{-4}$	2.5	3.0	3.1	3.3	3.7
σ	5.15–3.22	6.26–3.43	6.83–3.56	6.36–3.76	8.82–4.58
σ_i	4.71	4.44	4.52	4.42	5.17

Table 2. List of the examined PAM solutions with their main characteristics.

3. Description of the flow field

The flow path is schematically illustrated in figure 2. The coordinate system is located at the midspan of the channel, with the x-axis starting at the intersection point of the throat and the divergence zones of the nozzle and the y-axis starting from the channel's centreline and pointing vertically upward. Liquid flow of density ρ_L and temperature T_{in} enters the channel at pressure p_{in} and streamwise area-averaged velocity $\bar{\bar{u}}_{in}$ and leaves it at p_{out} and $\bar{\bar{u}}_{out}$. Single-point wall pressures at the top and bottom of the downstream flow are denoted as $p_{d,1}$ and $p_{d,2}$, respectively. The main dimensions of the flow path are annotated in figure 2.

In this paper, the time average of an arbitrary instantaneous scalar field $g(x, y, t)$ and its fluctuating component are denoted by $\langle g(x, y)\rangle$ and $g'(x, y, t)$, respectively. The spatial average of g in the y-direction and over a plane (cross-section or the midspan) are shown by $\bar{g}(x, t)$ and $\bar{\bar{g}}(t)$, respectively. In the straight tube section (see figure 1), characteristic velocity was obtained from the time-averaged flow rate $\langle\dot{V}\rangle$ as $\langle\bar{\bar{u}}_{tu}\rangle = \langle\dot{V}\rangle/A_{tu}$, where A_{tu} is the cross-sectional area of the tube. The Reynolds number of the straight tube is defined as $Re_{tu} = \langle\rho_L\rangle\langle\bar{\bar{u}}_{tu}\rangle D_{tu}/\mu_w(C_s)$, where $\langle\rho_L\rangle$ was determined using temporal measurements of the Coriolis flowmeter (Krohne Optimass 7000). Here, μ_w and C_s are the wall shear viscosity and polymer concentration in the solution, discussed in § 4.1. For the channel flow over the nozzle, illustrated in figure 2, the characteristic length was chosen to be the hydraulic diameter of the throat, $D_{h,th} = 2.86$ mm, and the characteristic velocity was $\langle\bar{\bar{u}}_{th}\rangle = \langle\dot{V}\rangle/A_{th}$. The Reynolds number based on the throat length scale and velocity is defined as $Re_{th} = \langle\rho_L\rangle\langle\bar{\bar{u}}_{th}\rangle D_{h,th}/\mu_w(C_s)$.

Cavitation number σ is defined as

$$\sigma = \frac{\langle p_{in}\rangle - p_{sat}\left(\langle T_L\rangle\right)}{0.5\langle\rho_L\rangle\langle\bar{\bar{u}}_{th}\rangle^2}, \tag{3.1}$$

where, $\langle p_{in}\rangle = \langle\Delta p_{ch}\rangle + \langle p_{out}\rangle$ is the time-averaged absolute pressure of a single point at the channel's inlet wall. Here, $\langle\Delta p_{ch}\rangle$ is the mean measured pressure drop over the channel and $\langle p_{out}\rangle$ is the mean absolute outlet pressure. The outlet valve, shown in figure 1, was entirely open during the experiments, resulting in a constant measured p_{out} varying in the range of 0 %–1 % below the atmospheric pressure in all tests. Vapour saturation pressure at the liquid's temperature $\langle T_L\rangle$ is denoted by p_{sat}, where $\langle T_L\rangle = 0.5(\langle T_{in}\rangle + \langle T_{ou}\rangle)$. Values of p_{sat} were determined using X Steam (Holmgren 2021), a code developed in MATLAB (2021; MathWorks). In this study, PAM additives (BASF SE; Germany) were used as cavitation and turbulent drag reduction agents. Semidilute mixtures of PAM and tap water at different concentrations were used as operating fluids in the system. Table 2 lists the range of the Re_{th} and σ and their associated values at the cavitation inception for the examined PAM solutions.

https://doi.org/10.1017/jfm.2022.910 Published online by Cambridge University Press

High-frequency pressure sensors located downstream of the flow (see figure 2) measured the pressure variation relative to an arbitrary initial reference value. Hence, their time-averaged value is of no significance. The r.m.s. of the downstream's fluctuating component of the single-point pressure signal $p'_{d,rms}$ expounds the intensity of pressure pulsation due to the collapse of cavitation bubbles. For brevity, results for sensors 1 and 2, shown in figure 2, are presented together. Here, the Strouhal number St is defined as

$$St = \frac{f\mathcal{L}}{\langle \bar{\bar{u}}_{th} \rangle}, \tag{3.2}$$

where, f is the maximum dominant pulsation frequency and $\mathcal{L}$ is the characteristic length scale of the flow system. In the current study, signals originating from pressure measurements were used to determine f.

4. Results and discussion

4.1. *Flow rheology*

The mass of the PAM required to prepare the desired solution concentration was measured using a digital scale (Explorer; Ohaus Corporation) with a 0.1 mg resolution. The additives were gradually added to a 0.5 L glass beaker filled with water and mixed using a stirrer (1103; Jenway) at a moderate constant rotational speed. The stirring bar size was selected to cover most of the container's surface to mitigate the adhesion of polymers to the container walls. Each master solution was stirred for two hours, and the resultant uniform, highly concentrated solution was then gradually added to the circulating water in the flow loop. The solution was allowed to circulate at a moderate pump speed for one hour, with the channel line bypassed, before doing any tests. Samples were obtained from the flow line using a sampling valve installed close to the channel's inlet (see figure 1). Later, the solution was undergone the most extreme cavitation scenario, and another sample was taken to explore the effect of cavitation on the rheology of the solution.

A short time after taking the samples, the rheological characteristics of the solutions were determined using a rotational rheometer (Kinexus lab+; NETZSCH-Gerätebau GmbH) with a double gap geometry (DG25). The bob's internal and external diameters were 23 and 25 mm, respectively, with an internal height of 57.5 mm. The cup had a diameter of 26.25 mm, and an insert diameter of 22 mm. Three independent measurements were performed for each sample at 20 °C with the shear rate controlled during the tests. The average measurement values, with corresponding standard deviations, are reported here.

Figure 4(*a*) shows the variation of the solution viscosities versus the strain rate. The results indicate that the selected PAM solutions in water have shear-thinning behaviour. Such a fluid behaves as a Newtonian fluid at very low, $\mu(\dot{\gamma} \ll 1) \rightarrow \mu_0$, and very high, $\mu(\dot{\gamma} \gg 1) \rightarrow \mu_\infty$, shear rates (Bird, Armstrong & Hassager 1987). Shear-thinning fluids follow a power law relation for intermediate $\dot{\gamma}$ values, i.e. $\mu = K\dot{\gamma}^n$ for $1 < \dot{\gamma} < \infty$ (Bird *et al.* 1987). Here, K and n are correlation constants. The standard deviation of the viscosity measurements were more than 10 % for $\dot{\gamma} < 10\,\mathrm{s}^{-1}$ and $\dot{\gamma} > 500\,\mathrm{s}^{-1}$ and hence were discarded. This discrepancy is caused by surface tension that produces artefact shear-thickening at low shear rates and the development of unstable secondary flows for higher shears, where viscosity shows a sudden increase (Morrison 1998). The Correau–Yasuda (CY) model (Yasuda, Armstrong & Cohen 1981) was fitted to the measurement data to determine the solution viscosities at higher strain rates, and the

https://doi.org/10.1017/jfm.2022.910 Published online by Cambridge University Press

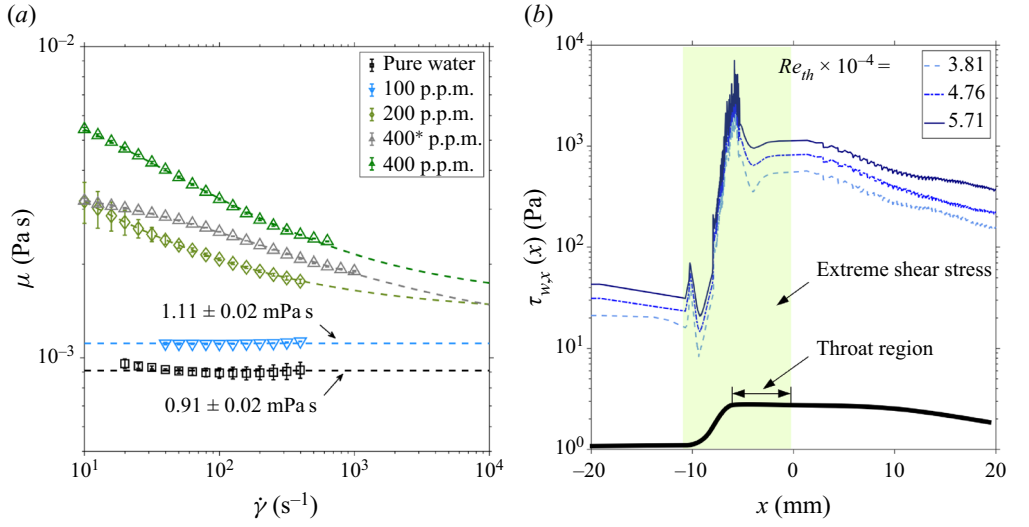

Figure 4. (*a*) Variation of the dynamic viscosity of the pure water and PAM solutions versus the shear rate. A dashed line depicts the fitted CY model for each solution with a concentration of more than 100 p.p.m. For pure water and the 100 p.p.m. solution, dashed lines show the average values in the span of the measured shear rates. The error bars indicate the standard deviations of three independent measurements. Here, '*' signifies that the solution has experienced the cavitation process. (*b*) Changes of the numerically determined (see Appendix A) wall shear stress in the streamwise direction $\tau_{w,x}(x)$ on the midspan of the channel in the pure water flow, plotted for three different Re_{th}. The inserted thick black curve illustrates the profile of the lower nozzle wall. A pale-green rectangle highlights the region of extreme shear stress.

results are plotted in figure 4(*a*) as dashed lines. The CY model is formulated as

$$\mu(\dot{\gamma}) = \mu_\infty + (\mu_0 - \mu_\infty)\left[1 + (\lambda_t \dot{\gamma})^a\right]^{(n-1)/a}, \tag{4.1}$$

where μ_0 and μ_∞ are the zero and infinite shear viscosities. Here, λ_t is a time constant, n is the power-law index and a is a constant parameter suggested by Yasuda *et al.* (1981). As discussed by Syed Mustapha *et al.* (1999) and later by Escudier *et al.* (2001), the Pearson correlation coefficient r should be more than 0.9975 for a rheological model to be valid and reliable. Here, r is (Escudier *et al.* 2001)

$$r = \frac{N\sum_{i=1}^{N}\mu_{M,i}\mu_{CY,i} - \sum_{i=1}^{N}\mu_{M,i}\sum_{i=1}^{N}\mu_{CY,i}}{\sqrt{\left[N\sum_{i=1}^{N}\mu_{M,i}^2 - \left(\sum_{i=1}^{N}\mu_{M,i}\right)^2\right]\left[N\sum_{i=1}^{N}\mu_{CY,i}^2 - \left(\sum_{i=1}^{N}\mu_{CY,i}\right)^2\right]}}, \tag{4.2}$$

where N denotes the total number of viscosity measurements and the subscript 'M' means 'measured'. The coefficient of determination R is also calculated for each solution to evaluate the accuracy of the utilized model. Table 3 lists the obtained coefficients of the CY model for each PAM solution, with their associated r and R coefficients. For all cases, $r > 0.9992$ and $R > 0.9985$; hence, the obtained correlations are valid for estimating the viscosity values at higher strain rates.

As figure 4(*a*) illustrates, the viscosity of the 400 p.p.m. solution decreases for the entire range of the tested shear strain rates after experiencing violent cavitation conditions.

https://doi.org/10.1017/jfm.2022.910 Published online by Cambridge University Press

C_s (p.p.m.)	μ_0 (mPa s)	μ_∞ (mPa s)	λ_t (s)	n	a	r	R
200	8.010	1.388	2.287	0.58	3.523	1.0000	0.9999
400*	3.616	1.137	0.033	0.66	0.693	0.9993	0.9983
400	8.395	1.525	0.164	0.53	0.732	0.9993	0.9987

Table 3. List of coefficients of the CY model for the tested PAM solutions, with their corresponding r and R coefficients. Here, '*' signifies that the solution has experienced the cavitation process.

While still showing shear thinning behaviour at relatively lower shear strain rates, the results suggest that the cavitation process weakens this behaviour. As given in table 3, the solution has an infinite viscosity of ≈18 % lower than the 200 p.p.m. solution that was not undergone the cavitation process. This result confirms that the polymers used in this work degrade mechanically due to the molecular scission at relatively large shear strain rates.

In this study, the mass flow rate was chosen as the independent parameter and was varied for each fluid to produce a range of flow conditions. Hence, Re_{th} was matched between different solution flows to investigate the effect of PAM additives on the cavitation process. As discussed, the PAM solutions are shear-thinning, and their local rheological behaviour in the flow domain depends on the strain rate they experience and the relaxation time of the solution. Therefore, to determine Re_{th} for PAM solutions, it is crucial to estimate the wall viscosity at the shear rate experienced by the throat wall, i.e. $\mu_{w,th}(\dot{\gamma}_{w,th})$. It was not feasible to resolve the viscous sublayer at the throat using the optical settings described in § 2.2. Therefore, $\dot{\gamma}_{w,th}$ was calculated using (1) the Prandtl–Kármán (PK) friction factor correlation (White 2011) for turbulent water flow in smooth tubes and (2) a three-dimensional numerical simulation of the turbulent water flow. Details of the numerical set-up are given in Appendix A. It is important to note that $\dot{\gamma}_{w,th}$ might change in a viscoelastic flow (Naseri *et al.* 2018), and more accurate simulations based on a non-Newtonian flow model are required to elucidate this conjecture. Nevertheless, the effect of this difference is negligible on Re_{th}. As an example, in the 400 p.p.m. solution, $\mu_{w,th}(5.0 \times 10^4\ \mathrm{s}^{-1}) = 1.627$ mPa s and $\mu_{w,th}(2.5 \times 10^4\ \mathrm{s}^{-1}) = 1.667$ mPa s. For this solution, at a constant flow rate, a 50 % reduction in the shear strain rate increases the wall shear viscosity and decreases Re_{th} by only 2.5 % in the highest PAM concentration tested. Hence, numerically obtained values of $\dot{\gamma}_{w,th}$ in water flow were used to approximate Re_{th} of PAM solutions prior to tests and to match them with Re_{th} of pure water flow.

Figure 4(*b*) depicts the variation of the wall shear stress $\tau_w(x)$ of pure water flow in the streamwise direction x at the midspan of the channel, obtained numerically for three different inlet flow rates. Water flow experiences extreme shear stress in the throat region, which increases for higher flow rates. Numerical wall shear stress values were averaged over the bottom flat plate of the throat region and were used to determine the average shear rate at the throat wall $(\dot{\gamma}_{w,th})_{CFD}$. Table 4 lists the calculated average shear stresses and their associated shear strain rates for three different Re_{th} of the pure water flow. The estimated values based on the PK friction factor are in the range of ±10 % of their numerical counterpart. Nevertheless, only the numerical values are used for further calculations.

A numerical parametric study was conducted with a similar set-up explained in Appendix A for five different inlet conditions in the range of $2 \times 10^4 < Re_{th} < 6 \times 10^4$ for pure water flow. The results were used to estimate the shear rate and viscosity at the

https://doi.org/10.1017/jfm.2022.910 Published online by Cambridge University Press

$\bar{\bar{u}}_{th}$ (m s^{-1})	$Re_{th} \times 10^{-4}$	$(\tau_{w,th})_{PK}$ (Pa)	$(\dot{\gamma}_{w,th})_{PK}$ (s^{-1})	$(\tau_{w,th})_{CFD}$ (Pa)	$(\dot{\gamma}_{w,th})_{CFD}$ (s^{-1})
13.34	3.8	494	543 000	448	492 300
16.67	4.8	734	807 000	772	848 700
20.01	5.7	1016	1 116 000	1076	1 183 000

Table 4. Calculated average wall shear stresses for three different throat velocities in pure water flow using the PK friction factor and three-dimensional numerical simulation. Here, $\langle \rho_L \rangle = 1000\,\mathrm{kg\,m^{-3}}$ and $\mu_{wat} = 0.91$ mPa s, the average measured water density and viscosity, were used in the calculations.

C_s (p.p.m.)	200		400*		400	
$\bar{\bar{u}}_{th}$ (m s^{-1})	$Re_{th} \times 10^{-4}$	$\mu_{w,th}$ (mPa s)	$Re_{th} \times 10^{-4}$	$\mu_{w,th}$ (mPa s)	$Re_{th} \times 10^{-4}$	$\mu_{w,th}$ (mPa s)
13.34	2.7	1.41	3.1	1.23	2.4	1.56
16.67	3.4	1.40	3.9	1.21	3.1	1.55
20.01	4.1	1.40	4.8	1.20	3.7	1.55

Table 5. Estimated average viscosities at the throat's wall and their corresponding Re_{th} for different flow rates, based on the numerical results of the pure water flow simulation. Here, '*' signifies that the solution has experienced the cavitation process.

throat wall. Table 5 lists the determined viscosities of different solutions at three throat velocities and equal $\dot{\gamma}_{w,th}$, with their associated Re_{th}. At relatively high shear rates experienced by the flow in this work, the largest $\mu_{w,th}$ is ≈1.56 mPa s, which is 1.7× larger than the pure water viscosity and belongs to the 400 p.p.m. solution at $\bar{\bar{u}}_{th} = 13.34\,\mathrm{m\,s^{-1}}$. All the reported Reynolds numbers in this study were calculated based on the average wall viscosity at that particular cross-section.

A series of oscillation frequency sweep tests using PAM solutions with concentrations of 50 to 400 p.p.m. were conducted and the resultant elastic (storage) modulus $G'(\omega)$ and viscous (loss) modulus $G''(\omega)$ are plotted in figure 5(*a*,*b*) as functions of angular frequency ω. The strain was kept constant at 1 % in all tests. As shown in figure 5(*a*), the elastic moduli of all tested solutions show a plateau for the range of $0.1 \lessapprox \omega \lessapprox 10\,\mathrm{rad\,s^{-1}}$ and start to increase as ω increases. An increase in the polymer concentration increases the plateau G'. As figure 5(*b*) illustrates, the viscous moduli changes almost linearly for $\omega \gtrapprox 10\,\mathrm{rad\,s^{-1}}$, which highlights the Newtonian behaviour of the fluid in this frequency range, i.e. $G'' = \mu_0\omega$, where the viscosity μ_0 shows an increase as the concentration increases. Oscillation tests were also conducted for higher frequencies to obtain the crossover points of $G'(\omega)$ and $G''(\omega)$ profiles. The crossover point correlates with the relaxation time t_R of the solution. For 200 and 400 p.p.m. solutions, $t_R \approx 14.5$ ms and $t_R \approx 12.5$ ms were obtained as the average of three independent tests. Due to inertial effects, no consistent crossover points were obtained for lower concentrations at higher frequencies.

4.2. *Drag reduction in non-cavitating tube flow*

Dimensionless pressure gradient or the Fanning friction factor in a straight tube, such as the one shown in figure 1, is defined as $c_f = 2\tau_w/\langle \rho_L \rangle \langle \bar{\bar{u}}_{tu} \rangle^2$, where the wall mean shear stress τ_w is a function of the time-averaged measured pressure drop $\langle \Delta p_{tu} \rangle$ over length $L_{tu} = 0.92$ m of the tube with $D_{tu} = 19$ mm. Therefore, $\tau_w = D_{tu}\langle \Delta p_{tu} \rangle / 4L_{tu}$, and the

https://doi.org/10.1017/jfm.2022.910 Published online by Cambridge University Press

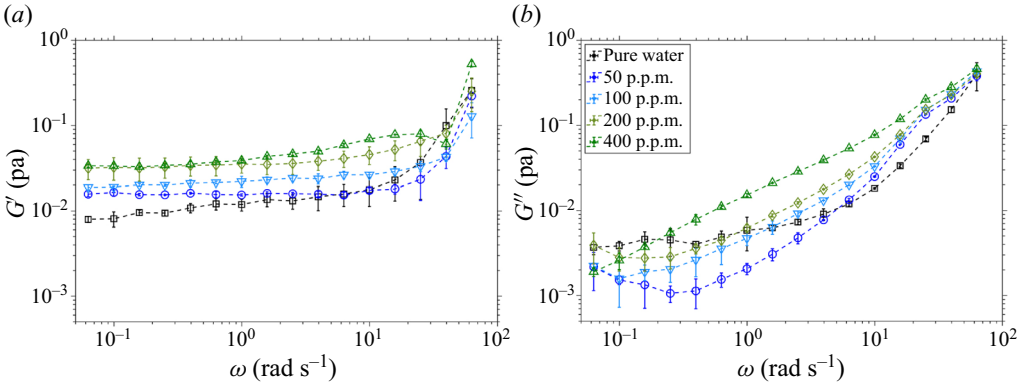

Figure 5. Changes of the (*a*) elastic (storage) modulus G' and (*b*) viscous (loss) modulus G'' of different PAM solutions with angular frequency ω. The strain rate was kept constant at 1 % and temperature at 20 °C in all tests. The plotted profiles are the average of three independent measurements and the error bars show the standard deviation of the measurements at each frequency.

Fanning friction factor can then be defined as

$$c_f = \frac{D_{tu}}{2L_{tu}} \frac{\langle \Delta p_{tu} \rangle}{\langle \rho_L \rangle \langle \bar{\bar{u}}_{tu} \rangle^2}. \tag{4.3}$$

Drag reduction (*DR*) is the relative reduction in the pressure drop of an additive solution over a known section of a flow path with a constant cross-sectional area compared with the pressure drop of the pure solvent flow at a similar flow rate (Lumley 1973; Virk 1975). Therefore, the percentage of *DR* can be defined as

$$DR\% = 1 - \frac{c_{f,s}}{c_{f,0}}, \tag{4.4}$$

where subscripts '*s*' and '0' stand for the additive solution and pure solvent, respectively. Here, c_f was calculated from the measured pressure drops in the turbulent flow of pure water and four different concentrations of PAM solutions in the range of $2 \times 10^4 \leq Re_{tu} \leq 3 \times 10^4$. Each test was repeated three times with a new solution, and the mean values are plotted in figure 6. The maximum standard deviation of the calculated friction factors was 7 % of its mean value. The resultant $c_f(Re_{tu})$ profile of pure water agrees with the PK equation (White 2011), shown with a dashed line in figure 6. Virk's asymptote for maximum drag reduction (MDR) (Virk, Mickley & Smith 1970) in dilute polymer solutions in turbulent pipe flow is indicated by a thick black line in figure 6. The MDR was not obtained for any of the tested solution concentrations. The 50 p.p.m. solution shows a higher *DR* (≈10 %–20 % more) than the 100 and 200 p.p.m. solutions. Increasing the concentration to 400 p.p.m. did not enhance pressure reduction, and a *DR* % comparable to the 50 p.p.m. solution was obtained for the tested flow rates. All examined concentrations resulted in a similar $DR \approx 50\,\%$ at the maximum tested flow rate ($Re_{tu} = 3 \times 10^4$).

The percentage ratio of instantaneous drag reduction, $DR(t)$ to the initial steady drag reduction of the system, DR_0, i.e. $(DR(t)/DR_0) \times 100\,\%$, was probed for a period of 500 s for different PAM solutions at $Re_{tu} = 3.0 \times 10^4$ to investigate the degradation level of the solutions. The results are plotted in figure 7. As shown, after ≈8 min, $DR(t)$ drops only by ≈5 % at maximum relative to its corresponding DR_0. The data acquisition for each test took nearly 10 s, and each solution was used only for four to five tests. The solution was

https://doi.org/10.1017/jfm.2022.910 Published online by Cambridge University Press

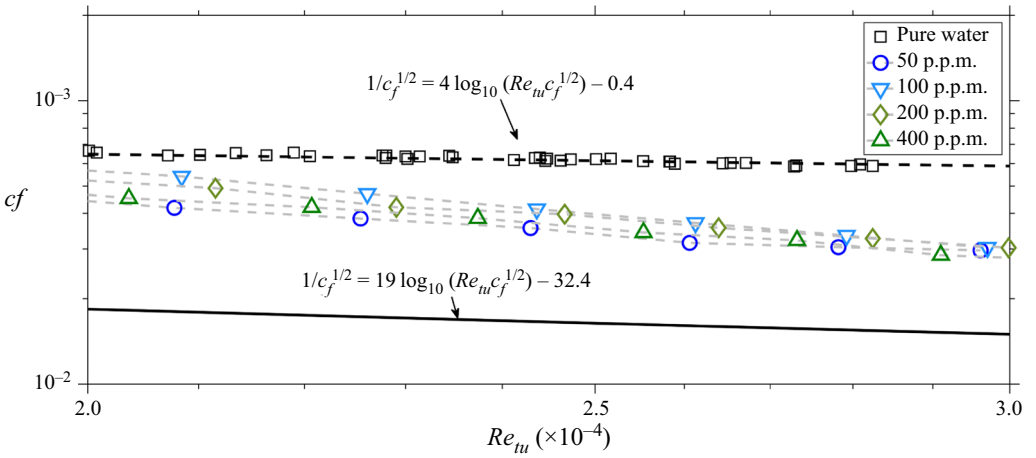

Figure 6. Variation of the Fanning friction factor, c_f, as a function of the straight tube's Reynolds number, Re_{tu}, in PAM solutions of various concentrations. The thick dashed line indicates the PK friction factor (White 2011) for turbulent water flow in smooth tubes. Virk's MDR asymptote (Virk *et al.* 1970) for turbulent flow of dilute polymer solutions in smooth tubes is shown by the solid black line. Each point on the plot denotes the mean of three independent measurements, with a maximum standard deviation of 7 % of the mean value in all tests.

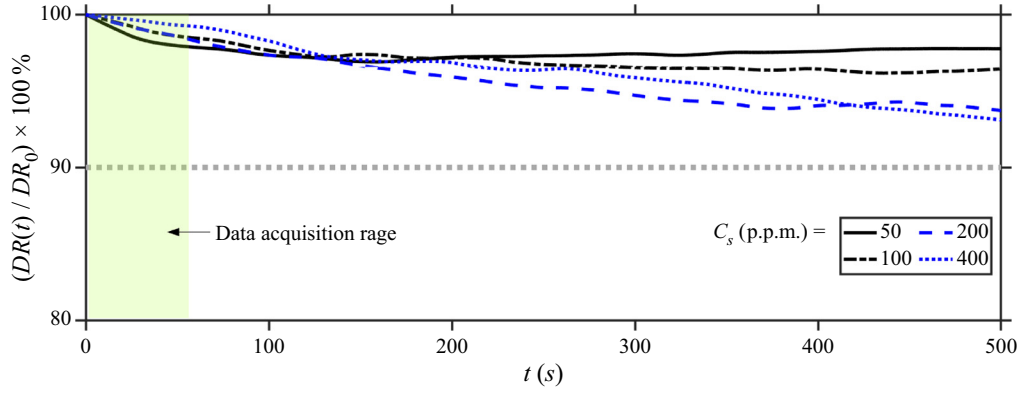

Figure 7. Degradation of the PAM solutions in time defined as the percentage ratio of the instantaneous drag reduction $DR(t)$ to the steady drag reduction of the flow system DR_0. Tests were conducted at $Re_{th} = 3.0 \times 10^4$.

renewed if further tests were required. A pale-green rectangle highlights the maximum data acquisition period with each fresh solution batch (≈50 s).

4.3. *Effect of polymer additives on the pressure drop over the nozzle*

As illustrated in figure 1, pressure drop was measured over the nozzle channel section using a differential pressure transducer. The pressure drops were measured for four different concentrations of PAM solution and pure water in the range of $2 \times 10^4 < Re_{th} < 6 \times 10^4$ to investigate the effect of PAM additives on nozzle flow. The results are plotted in figure 8(*a–d*) as $\sigma\,(Re_{th})$ profiles.

For pure water profiles in figure 8(*a–d*), σ decreases exponentially as the flow rate increases. After the onset of cavitation, σ drops with a smaller slope and approaches a

https://doi.org/10.1017/jfm.2022.910 Published online by Cambridge University Press

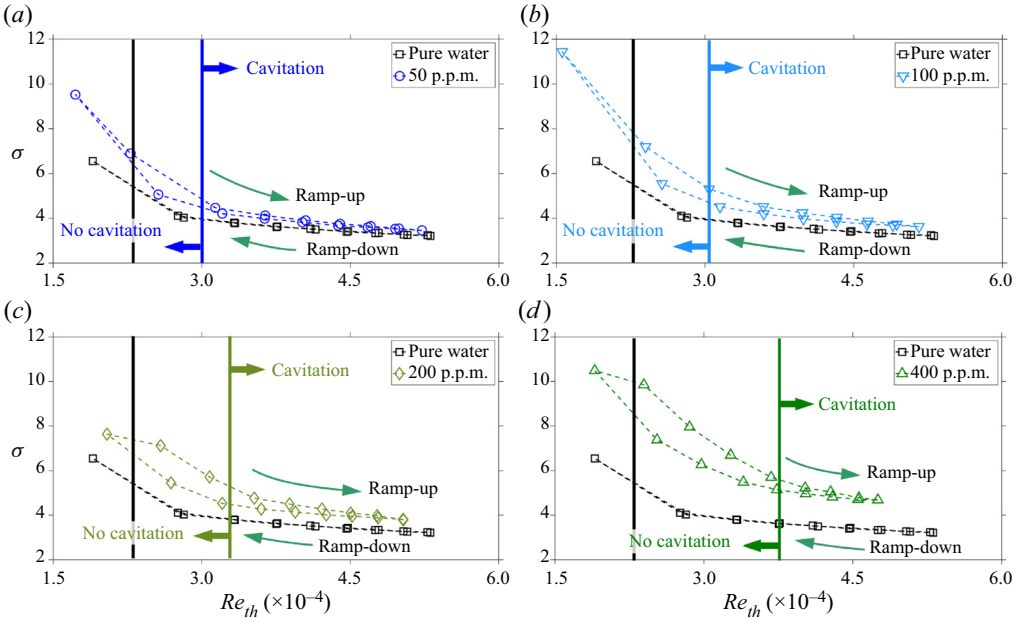

Figure 8. Variation of the cavitation number σ versus the throat Reynolds number Re_{th} for ramp-up (increasing Re_{th}) and ramp-down (decreasing Re_{th}) tests for (*a*) 50 p.p.m., (*b*) 100 p.p.m., (*c*) 200 p.p.m. and (*d*) 400 p.p.m. PAM concentrations. The cavitation onset points are shown by vertical solid lines coloured according to the colour code used for each solution concentration in the plots.

value of $\sigma \approx 3.2$ for higher Re_{th}. The gradual decrease of the water flow rate during the ramp-down test results in similar pressure drops over the nozzle. Figure 8(*a*) shows that the 50 p.p.m. solution results in a higher σ than the pure water flow at an equal Re_{th}. This difference decreases as the flow rate increases and cavitation intensifies. In the 50 p.p.m. solution, cavitation occurs at a flow rate ≈20 % higher than the pure water flow. As shown in figure 8(*b–d*), an increase in the solution concentration shifts σ to even higher values, and cavitation onset occurs at higher flow rates than the pure water flow.

For the tested concentrations, solution flows show higher levels of σ during a ramp-up test than in a ramp-down test. As figure 7 illustrates, it is possible that polymers experienced mild degradation while recirculating in the flow loop. Relatively, under cavitating flow conditions, it is highly probable that the rate of polymer degradation increased significantly due to the presence of extreme shear stress fields in cavitating regions. At the end of the ramp-up test, the solutions experience relatively high shear stresses during an intense cavitation process, which may cause elongated polymer molecules to degrade or entangled molecules to straighten. As figure 4(*a*) and figure 8(*a–d*) illustrate, the transmutation of the polymer molecules due to violent cavitation and extreme shears causes a local reduction in viscosity and pressure. Hence, the ramp-down tests show lower pressure drops than the ramp-up measurements.

Figure 9(*a*) compares the variation of σ of the solutions examined in this study during the ramp-down test. The inception Reynolds number $Re_{th,i}$ increases as the PAM concentration increases. For the maximum tested flow rate, corresponding to $Re_{th} \approx 5.4 \times 10^4$, pressure drop over the nozzle increases by ≈9 %, ≈13 %, ≈20 % and ≈50 %, respectively, in the 50, 100, 200 and 400 p.p.m. solution flows relative to the pure water flow. At the inlet of the nozzle channel, the wall shear stress is $O(10^2$ Pa) (see figure 4*b*),

https://doi.org/10.1017/jfm.2022.910 Published online by Cambridge University Press

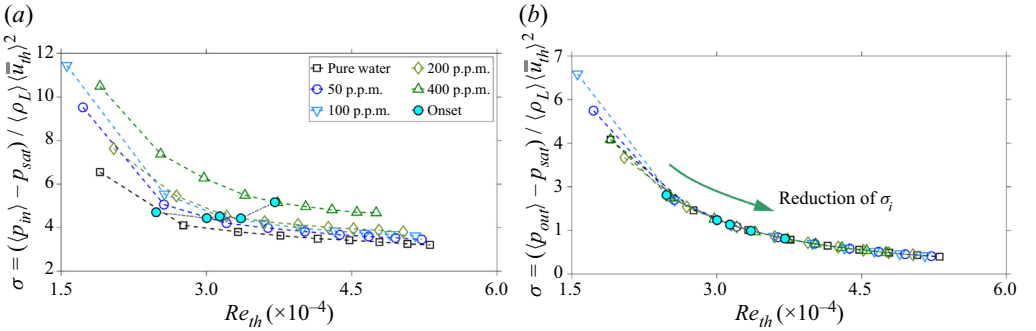

Figure 9. Changes of σ as a function of Re_{th} for different concentrations of PAM solutions for the ramp-down tests when (*a*) inlet pressure $\langle p_{in}\rangle$ and (*b*) constant outlet pressure $\langle p_{out}\rangle$ is selected as the reference pressure in (3.1). Cyan circles highlight the cavitation onset and σ_i denote the incipient cavitation number.

and its corresponding apparent shear viscosity in a PAM solution is higher than the pure water. Therefore, non-Newtonian PAM solutions have the potential to produce higher local pressures at low shear regions in the flow, such as the inlet of the nozzle in this study. This result agrees with the Δp_{ch} measurements in figure 8(*a–d*). The PAM concentration increases Δp_{ch} and accordingly inlet pressure p_{in} increases. It is important to note that p_{in} was intentionally chosen as the characteristic pressure in the definition of the cavitation number given in (3.2) to demonstrate the physical increase of the pressure drop over the curved nozzle. Yet, most of the previous studies on cavitation in non-Newtonian viscoelastic flows have used a constant reference pressure such as a free stream or outlet pressure to define the cavitation number (Hoyt 1976; Ōba *et al.* 1978; Hasegawa *et al.* 2009) and reported reductions in the incipient cavitation number σ_i of viscoelastic solutions relative to pure water. Therefore, as figure 9(*b*) shows, if the constant outlet pressure $\langle p_{out}\rangle$ is used in (3.1), σ_i demonstrates a reduction as the concentration increases.

4.4. *Temporal evolution of cavitation structures in pure water*

The cavitation onset is followed by a complex spatial and temporal evolution of cavitation structures, which expand in size as the pressure drop increases over the nozzle. Figure 10(*a–c*) illustrates four instantaneous sample snapshots of vapour ratio fields of cavitating pure water flow for three different flow conditions. These fields are projected on the channel's midspan plane and cover a FOV from approximately the end of the throat region to the vicinity of the end limit of the divergence region (see figure 2). For the current test conditions, the incipient cavitation number of pure water was $\sigma_i \approx 4.71$, which was associated with the emergence of tiny cavitation bubbles, detectable by the optical system described in § 2.2.

Figure 10(*a*) shows the vapour area ratio snapshots at $\sigma \approx 4.23$, with a flow rate of $\approx$16 % higher than the inception. Cavitation bubbles are produced cyclically from the top or bottom throat wall surfaces at this flow condition. As cavities elongate on the upper wall, relatively smaller jet clouds are produced on the lower wall and *vice versa*. Cavities detach from the end of the throat when they reach a length of $\approx 2h_{th}$ and flow downstream as they rapidly disintegrate and collapse into micron-sized bubbles. Most tiny micro cavitation bubbles collapse entirely, and any remnants are carried downstream by the bulk liquid flow. The cavity developed from one wall sporadically interacts with the passing jet cloud originating from the other and generates circular rolling clusters of cavitation bubbles with an equivalent diameter of $\approx h_{th}$. As the bubble clusters flow downstream, they

https://doi.org/10.1017/jfm.2022.910 Published online by Cambridge University Press

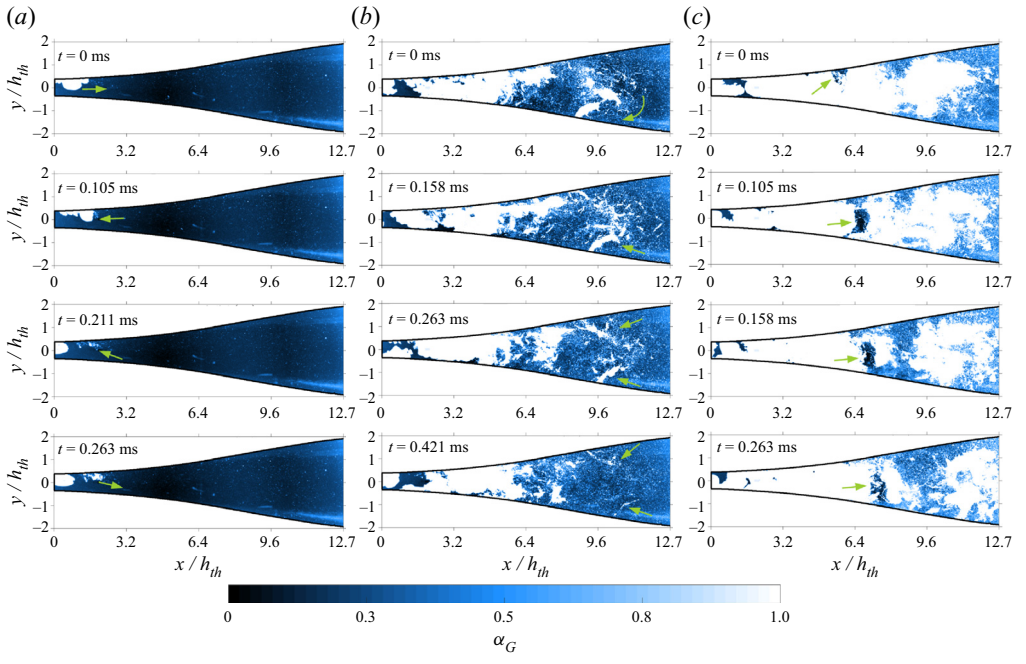

Figure 10. Snapshots of instantaneous cavitating pure water structures at (*a*) $Re_{th} = 2.9 \times 10^4$, $\sigma = 4.23$, (*b*) $Re_{th} = 3.8 \times 10^4$, $\sigma = 3.61$ and (*c*) $Re_{th} = 4.5 \times 10^4$, $\sigma = 3.37$, projected on the channel's midspan (plane $z = 0$). The white colour ($\alpha_G = 1$) shows the cavitation areas, and the black colour ($\alpha_G = 0$) demonstrates the bulk liquid. Sample growing and collapsing structures are annotated using green arrows. For related videos of (*a–c*), refer to movies 1–3 available at https://doi.org/10.1017/jfm.2022.910.

collapse in several microseconds and vanish entirely. Cavity clouds rebound several times during the collapse process and produce radially propagating pressure waves. Interaction of the pressure waves with the growing upstream cavities generates pockets of collapsing bubbles at the front of the cavities, which transmutes the cavity into an unstable transient structure.

Further increasing the flow rate enhances the cavitation process by causing larger pressure drops over the nozzle. Figure 10(*b*) illustrates snapshots of the cavitation structures at $\sigma = 3.61$ for the pure water flow. Here, developing cavities gain lengths up to $\approx 5h_{th}$ before they depart from their origins in the throat. Detached cavities decelerate as they flow downstream and are followed by the next generation of developing cavities. With $p(\boldsymbol{x}, t) \ll p_{sat}$ at almost any position close to the throat, the new-born cavities grow fast and finally bond with the just detached cavities. This bonding further fluctuates the large cavitation structure and may break it off into patches of collapsing streaky clusters of bubbles. These streaky structures exist only for several milliseconds before they entirely vanish or fall apart into micron-sized cavitation bubbles. The collapse of tilted streaky bubble pockets generates a series of shockwaves that propagate upstream and break the large structures of agglomerated packets of bubbles by modifying their local pressures. This process repeats itself with a particular frequency in time. The pressure field is highly unstable at the throat's downstream region and locally fluctuates around p_{sat}. As a result, smaller scales of bubble pockets emerge and instantly vanish at random positions in the downstream flow field. Chains of bullet-like bubbles are produced at the throat at irregular intervals, separated by liquid slugs of widths of $\approx 0.2h_{th}$. Thin films of lubricating liquid were also observed between the cavitation bullet-like bubbles and the channel's walls.

https://doi.org/10.1017/jfm.2022.910 Published online by Cambridge University Press

As these bubbles travel downstream, they collide with their preceding decelerated bubbles. As a result, they accumulate in this region and extend the cavitation body from its rear as its front collapses.

Figure 10(*c*) is associated with the instantaneous vapour ratio fields of the cavitating water flow with $\sigma = 3.37$. Huge pressure drops over the nozzle generate cavitation superstructures with oscillating lengths of $\approx 12h_{th}$ in the flow field. Even in this extreme condition, growing wall cavities cannot entirely occupy the core of the throat's exit region, which is dominated by a high-speed flow of the bulk liquid. Wall cavities expand, merge at the entrance of the divergence region and transform into cavitation superstructures. Interaction of the travelling shockwaves with the front of these huge clouds breaks them off into scattered clouds of cavitation bubbles. At this flow condition, the cloud cavitation collapse is chaotic and occurs at random positions in the flow field. As the clouds approach the maximum cross-sectional area, higher pressure levels ($p(\boldsymbol{x}, t) \gg p_{sat}$) shatter the bubble networks, and the fragmented bubbles vanish as they shrink in size and leave the channel. The chaotic cavitation escalates the dynamic pressure fluctuations, which intensifies the cavitation, and this cycle repeats itself as the upstream energy source is present.

As listed in table 2, a series of experiments using varying concentrations of PAM solutions in water were conducted to investigate the effect of PAM additives on the cavitation mechanism and explore the feasibility of the CR effect of these additives. Snapshots of instantaneous vapour ratio fields of the 200 p.p.m. solution on the channel's midspan are plotted in figure 11(*a–c*) for low, medium, and high-intensity cavitation conditions to illustrate the effect of PAM additives on the temporal evolution of cavitation structures. The cavitation process initiates at a Re_{th}, $\approx 32\,\%$ higher than the cavitation onset of the water flow.

As figure 11(*a*) illustrates, at a condition with a flow rate of only 6 % higher than the onset, the produced cavities form streaky topologies with wiggling outlines in the 200 p.p.m. solution. The instantaneous length of the streaky bubbles increases up to $\approx 2h_{th}$, with a length-to-width ratio of ≈ 6. At infrequent periods, the dominant core liquid flow is discontinued instantly by the merging wall cavities at the region where the wall profiles begin to diverge. As the fronts of the cavities break off, relatively uniform structures of detached cavities are generated. They oscillate, partially rebound and collapse as lumps of densely packed cavities, which emerge as continuous cavitation structures in the recorded images. Long polymer molecules act as flexible dampers in the flow field and relax extreme pressure field oscillations adjacent to the collapsing bubbles by releasing their stored energy under tension and storing energy under compression. This effect eases the cavitation process, increases the rebounding period of cavitating bubbles, and imposes lower pressure fluctuations on the surrounding bulk flow.

For the flow condition with $Re_{th} = 3.6 \times 10^4$, $\sigma = 4.37$, shown in figure 11(*b*), the core liquid flow exists only to a length of $\approx 2.5h_{th}$, the position where the growing wall cavities merge. A high-velocity thin layer of lubricating liquid flows upstream between the channel walls and the growing cavities. These continuous film flows possess high levels of momentum, and as they approach the throat, they come to a complete stop near the oncoming growing cavity. The interaction of the front of the lubricating films with the cavities transfers momentum to the cavities, lifts them in the positive wall-normal direction, and separates them from the channel walls. This phenomenon accelerates the merging of the cavities. The recirculating flow regions trap the detached collapsing cavities at irregular periods in the downstream flow field. As a result, the collapse rate is enhanced in regions with a recovered pressure, where the cavities attune to the pressure distribution patterns in the recirculating region by altering their topology.

https://doi.org/10.1017/jfm.2022.910 Published online by Cambridge University Press

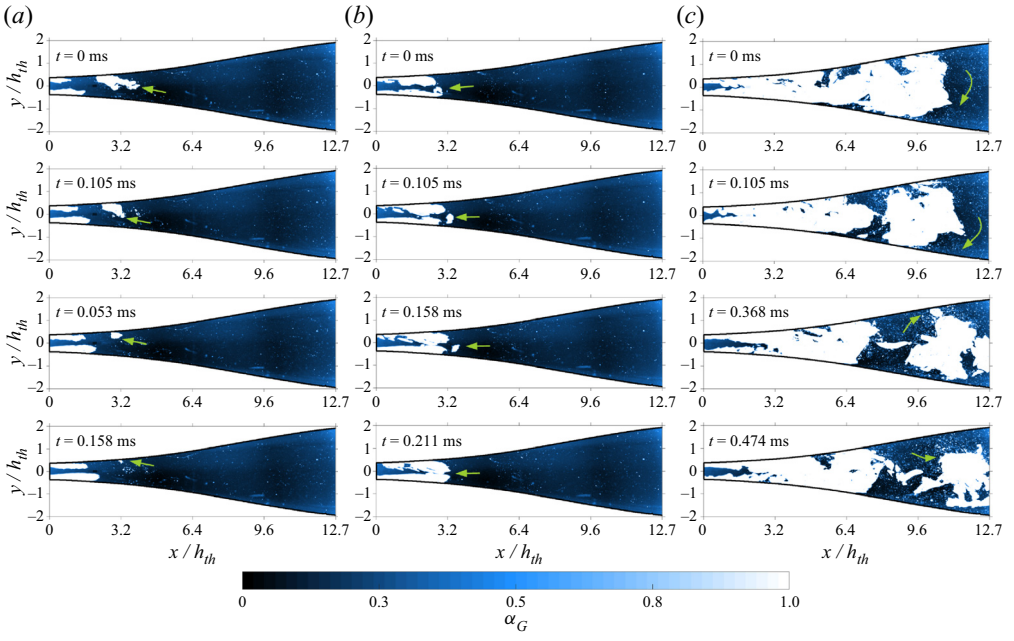

Figure 11. Snapshots of instantaneous cavitating structures in 200 p.p.m. PAM solution flow at (*a*) $Re_{th} = 3.5 \times 10^4$, $\sigma = 4.48$, (*b*) $Re_{th} = 3.6 \times 10^4$, $\sigma = 4.37$ and (*c*) $Re_{th} = 4.3 \times 10^4$, $\sigma = 4.00$, projected on the channel's midspan (plane $z = 0$). The white colour ($\alpha_G = 1$) shows the cavitation areas, and the black colour ($\alpha_G = 0$) demonstrates the bulk liquid. Sample growing and collapsing cavitation structures are annotated using green arrows. For related videos of (*a–c*), refer to movies 4–6.

As figure 11(*c*) illustrates, cavitation clouds develop into immense structures downstream at a higher cavitation level. The visualization results indicated that the developed cavities remained attached to the wall surfaces during the entire recording time. Under this condition, small-scale clouds were produced due to the break-off and chaotic collapse of the front of the developed cavities, which shed downstream. These clouds show random topologies and generate mesoscale clusters of cavitation bubbles as they collapse. In contrast to pure water flow (see figure 10*c*), where the collapse of shedding small-scale cavitation clouds downstream produced consistent micron-sized bubbles, the 200 p.p.m. solution flow produced mesoscale bubble networks with sizes in the range of ≈0.2–0.5 mm.

Instantaneous snapshots of cavitating flow structures at the convergence and throat regions of different PAM solution flows are illustrated in figure 12(*a–c*) at three different Re_{th}. As seen, cavitation structures emerge on the walls at about $x/h_{th} \approx -1$, adjacent to the midway of the throat region, oscillating on both walls cyclically as they grow downstream. As expected, increasing the PAM concentration reduces the cavitation intensity and suppresses it at higher concentrations for the tested flow conditions.

Spatiotemporal maps of cavitating flow fields were evaluated to demonstrate the CR effect of PAM additives on the temporal evolution of cavitation structures. These fields were obtained by averaging each instantaneous vapour ratio field relative to the *y*-direction, i.e. $\bar{\alpha}_G(x, t)$, and stitching the resultant lines chronologically. The results are shown in figure 13(*a,b*) for an intermediate and a high flow rate of pure water flow and four different concentrations of PAM additives for 45 ms. The PAM additives demonstrate significant

https://doi.org/10.1017/jfm.2022.910 Published online by Cambridge University Press

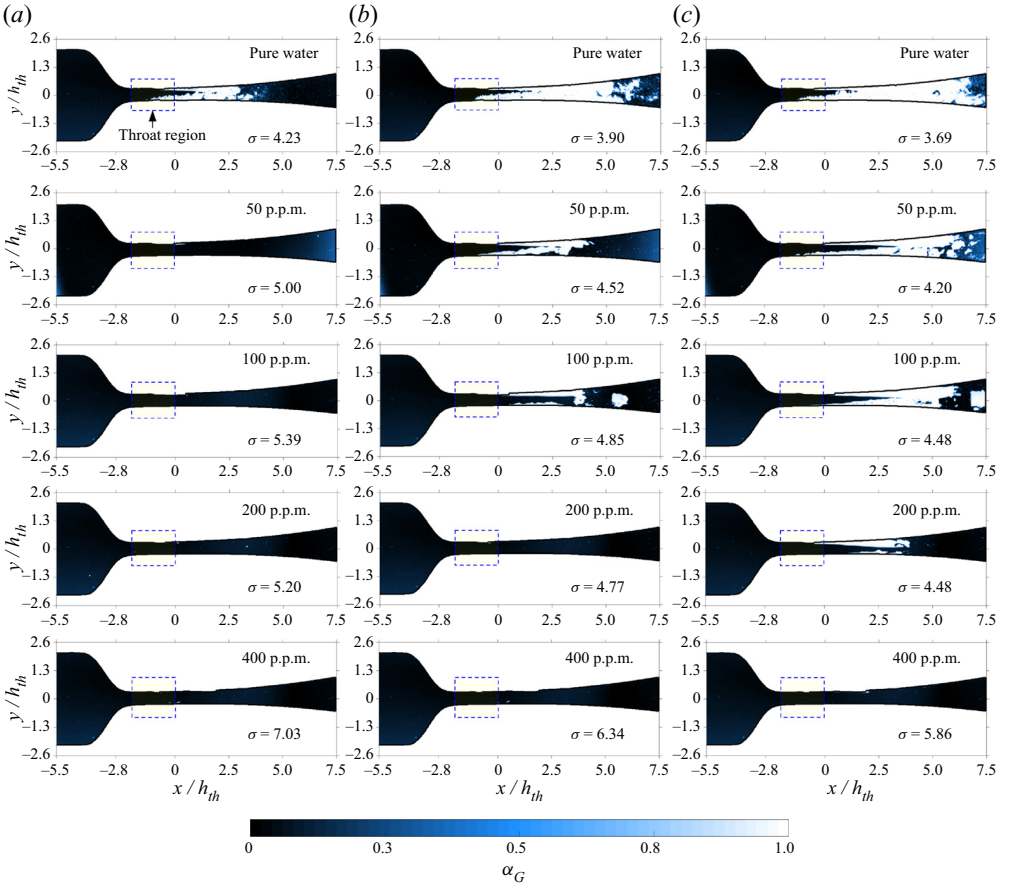

Figure 12. Snapshots of instantaneous vapour ratio fields in different PAM solution flows at the convergence and throat regions for (*a*) $Re_{th} = 2.6 \times 10^4$, (*b*) $Re_{th} = 3.0 \times 10^4$ and (*c*) $Re_{th} = 3.4 \times 10^4$, projected on the channel's midspan (plane $z = 0$). The white colour ($\alpha_G = 1$) shows the cavitation areas, and the black colour ($\alpha_G = 0$) demonstrates the bulk liquid. The flow direction is from left to right and a pale-yellow rectangle, with dashed blue borders, signifies the throat region on each figure. For sample videos, refer to movies 7–8.

CR effects by strongly relaxing the chaotic unstable cavity fronts, attenuating their growth downstream, and suspending the cavitation onset to higher Re_{th}. As given in table 2, cavitation initiates at $Re_{th,i} = 3.7 \times 10^4$ in the 400 p.p.m. solution, which is ≈50 % higher than $Re_{th,i}$ of pure water.

In figure 13(*a*), the front of the vaporous structures in the 50 p.p.m. solution flow oscillates with a mean length similar to that in pure water. The population of the miniature cavitation bubbles swimming at the closure of the cavity in the pure water flow is strongly alleviated in the 50 p.p.m. solution. In pure water, the footprints of these tiny bubbles are visible as irregular fading regions of $\bar{\alpha}_G$ at the cavity closure, which are moderated in the 50 p.p.m. solution flow, as shown in figure 13(*a*). At $Re_{th} = 3.4 \times 10^4$, a further increase of the PAM concentration suppresses the cloud cavitation by damping the growth of the wall cavities and retarding them to sheet cavities. Cavitation is entirely suppressed for a 400 p.p.m. solution, with the only infrequent appearance of small evanescent cavities.

https://doi.org/10.1017/jfm.2022.910 Published online by Cambridge University Press

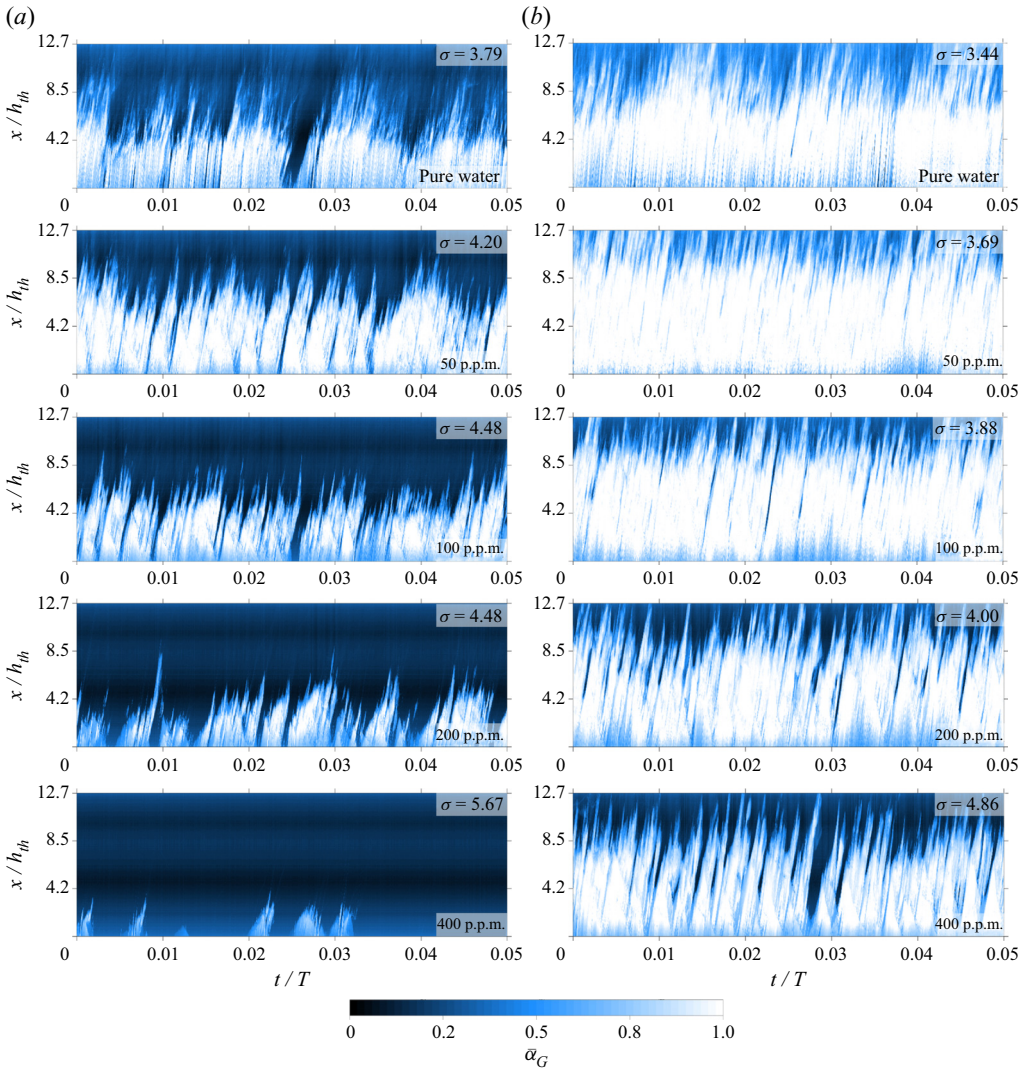

Figure 13. Spatiotemporal fields of cavitating PAM solutions for (*a*) $Re_{th} = 3.4 \times 10^4$, and (*b*) $Re_{th} = 4.4 \times 10^4$. Each row corresponds to a different concentration. From top to bottom, results for pure water, 50, 100, 200 and 400 p.p.m. solutions are illustrated, respectively. From the total imaging period of $T = 0.895$ s, only 45 ms is illustrated for each flow condition.

Under extreme cavitation conditions, as shown in figure 13(*b*), large-scale cavitation structures shed downstream, filling almost the entire visualized FOV. At this relatively high flow rate, the 50 p.p.m. solution displays an even more intense cavitation process than the pure water, enhancing the cavitation instead of reducing it. As the solution concentration increases to 100 p.p.m., the relatively tiny cavitation bubbles adjacent to the oscillating cloud fronts fade out. Growing cavities maintain lengths of similar scales to that in the pure water flow while oscillating periodically, with lower fluctuations relative to the average cavity length. As figure 13(*b*) illustrates, increasing the concentration to even 400 p.p.m. cannot suppress the vivacious cavitation structures at this flow condition and only linearize the growth rate of the cloud cavities in time. Once a cavity begins to

https://doi.org/10.1017/jfm.2022.910 Published online by Cambridge University Press

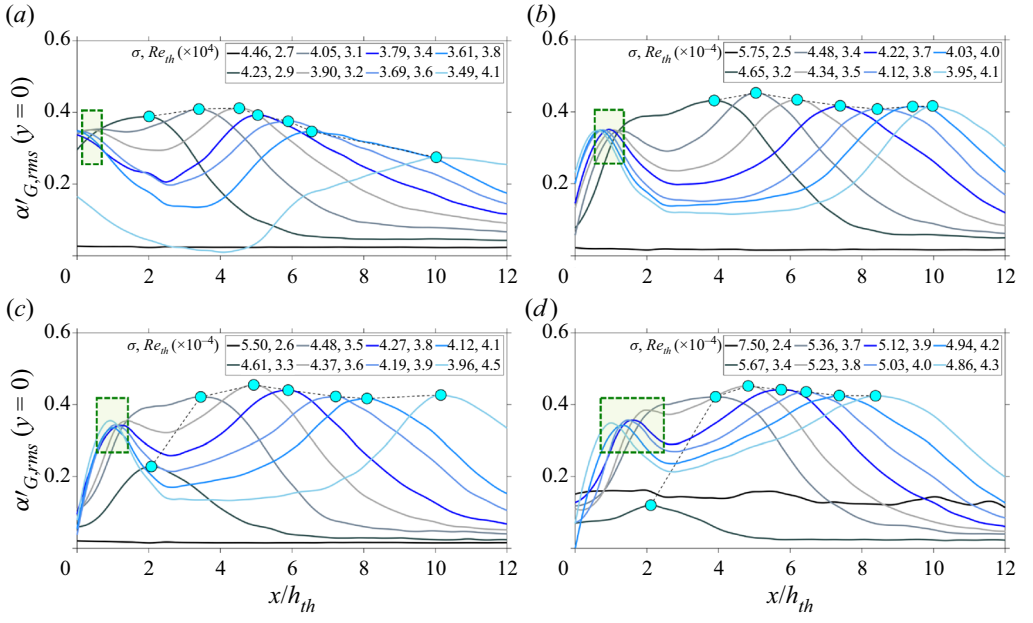

Figure 14. Variation of the cavitation intensity $\alpha'_{G,rms}$ on the midspan plane $z = 0$ and at the channel's centreline $y = 0$, for the selected range of flow conditions with increasing Re_{th} and decreasing σ for (*a*) pure water, (*b*) 100 p.p.m., (*c*) 200 p.p.m. and (*d*) 400 p.p.m. solution flows. The positions of $[\alpha'_{G,rms}(y = 0)]_{max}$ are highlighted with cyan circles on each figure and connected with a black dashed line to demonstrate the variation of the maxima. The regions of cavitation detachment adjacent to the throat are emphasized using rectangles coloured in pale-green with dashed dark green outlines.

grow, it expands at an almost constant rate to its maximum length, comparable to the entire length of the divergence region downstream, then it dwindles at a constant and relatively steeper rate, and this process repeats itself in time. Conversely, as the vaporous structures grow in the pure water flow at this high flow rate, they shrink and grow sporadically, at a time-dependent random rate, and produce significant batches of micron-sized dispersed bubbles, which swim in their vicinity and dispense in the entire downstream region.

4.5. *Cavitation length*

The r.m.s. of the fluctuating component of the vapour ratio field $\alpha'_{G,rms}$ was calculated for each flow condition to quantify the cavitation intensity. A set of ≈17 000 images were analysed for each flow case to ensure the values converged statistically. Figure 14(*a–d*) show the variation of $\alpha'_{G,rms}$ in the streamwise direction, downstream of the throat on the $y = 0$ centreline of the midspan plane, for different flow conditions and PAM solutions. Each $\alpha'_{G,rms}(y = 0)$ profile demonstrates a peak, which is associated with the mean position of the oscillating cavitation front. The streamwise distance of this point relative to the origin at $x = 0$ characterizes an appropriate length scale for cavitation structures, denoted by L_{ca} in this study. Dular *et al.* (2004) and Zhang *et al.* (2019), among others, used a similar approach to measure the cavitation length. The loci of the peak points are highlighted by cyan circles on the plots in figure 14(*a–d*). There is another peak present in each $\alpha'_{G,rms}(y = 0)$ profile in the $x < 2h_{th}$ region. This point corresponds to the mean streamwise position, where cavities detach from the wall surfaces. In figure 14(*a–d*), these detachment regions are highlighted by green dashed rectangles.

https://doi.org/10.1017/jfm.2022.910 Published online by Cambridge University Press

Figure 14(*a*) shows that as the flow rate (equivalently the pressure drop) of the pure water flow increases, cloud cavitation structures develop into a wider region downstream while maintaining a maximum of $\alpha'_{G,rms} \approx 0.42$ until $Re_{th} = 3.9 \times 10^4$ and $\sigma = 3.2$. After this point, the maximum intensity decays linearly with increasing Re_{th}. This reduction in the maximum intensity reveals that the cavitation cloud's oscillating front is more stable at higher flow rates. For water flows with $\sigma < 3.2$, the growing cavities detach from the wall surface after a partial expansion and are transferred by the bulk liquid flow farther downstream, where they collapse due to pressure recovery. At the same time, new cavities are generated and develop from the throat when bulk liquid fills the collapse region. Therefore, α_G shows high fluctuations in this region, resulting in a higher $\alpha'_{G,rms}$ at the cloud's closure region. For $\sigma > 3.2$, the detachment and collapse periods are longer for larger, more violent structures. The flow region is repeatedly filled with newly growing cavitation bubbles, which statistically increases the probability of the existence of bubble pockets of a similar population in the same region. Therefore, the flow experiences lower fluctuation levels of α_G at the edge of the cavitation structures.

Similar to the pure water flow shown in figure 14(*a*), intensity values on the centreline of PAM solutions, given in figure 14(*b–d*), show two peaks: (1) in the close vicinity of the throat, where the clouds detach from the surface; and (2) at the edge of the cavitation clouds, where the cavity closure oscillates periodically. Maximum cavitation intensity is maintained for the full range of the examined Re_{th} and σ for PAM solutions tested, while its position is shifted farther downstream as Re_{th} increases. As a result, the addition of PAM polymers intensifies the fluctuations of the cavitation edge at higher flow rates, while relative to the pure water, they delay the cavitation onset to larger Re_{th}, and damp the expansion of the cavitation structures in the streamwise direction. Figure 14(*a*) reveals that the cavitation detachment position remains almost constant for the entire range of the tested flow rates for pure water at $x/h_{th} \approx 0.4$. Conversely, as shown in figure 14(*b–d*), rising the concentration level in the solution generally shifts the detachment position downstream, respectively, to $x/h_{th} \approx 1.0$, $x/h_{th} \approx 1.2$ and $x/h_{th} \approx 1.8$. However, as Re_{th} increases, the mean detachment position reverses towards upstream.

The estimated cavitation lengths based on the loci of $[\alpha'_{G,rms}(y = 0)]_{max}$ are plotted in figure 15(*a*,*b*) for varying Re_{th} and σ and different solutions of PAM in water. As shown in figure 15(*a*), the occurrence of the minimum cavitation length $L_{ca,min} \approx 2h_{th}$ is shifted towards higher Re_{th} and σ as the concentration increases. For the 400 p.p.m. solution, this happens at a Re_{th} of ≈18 % higher than pure water. For all examined solutions, L_{ca} increases almost linearly with Re_{th}. At relatively higher flow rates, $3.2 \times 10^4 < Re_{th} < 4.0 \times 10^4$, 50 and 100 p.p.m. solutions expand to longer cavitation structures than pure water, enhancing the growth of streaky and cloud cavities. Solutions with concentrations of more than 100 p.p.m. decelerate the expansion of the cavitation clouds and shrink their size in the streamwise direction. For instance, at $Re_{th} = 4 \times 10^4$, L_{ca} in the 400 p.p.m. solution is reduced by 30 % relative to pure water.

As shown in figure 15(*b*), cavitation length increases almost linearly with the reduction of σ for all examined solutions. A similar L_{ca} is generated at a higher σ in PAM solutions relative to pure water. A cavity of $L_{ca,min} \approx 2h_{th}$ occurs at $\sigma \approx 5.7$ in the 400 p.p.m. solution, which is ≈34 % higher than its counterpart in pure water. There is a noticeable shift (≈11 %) in the $L_{ca}(\sigma)$ profile for the 50 p.p.m. solution compared with pure water. Increasing the mixture concentration from 50 to 200 p.p.m. does not indicate a significant shift in $L_{ca}(\sigma)$. As the PAM concentration increases to 400 p.p.m., $L_{ca}(\sigma)$ shifts ≈23 % towards higher σ when compared with the 50–200 p.p.m. profiles. These shifts follow the increase of the inlet pressure due to the local increase of the solution's shear viscosity discussed in § 4.1.

https://doi.org/10.1017/jfm.2022.910 Published online by Cambridge University Press

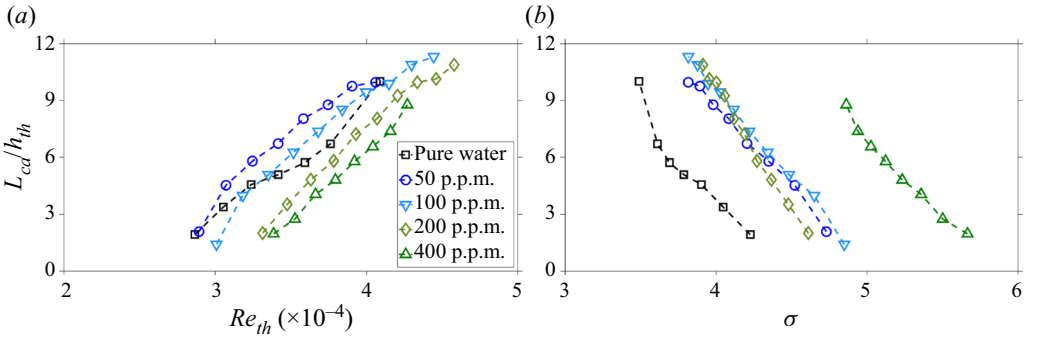

Figure 15. Variation of the normalized cavitation length with (*a*) throat Reynolds number Re_{th} and (*b*) cavitation number σ for pure water and four different concentrations of PAM solution in water.

4.6. *Temporal variance of cavitation structures*

In an instantaneous image captured from a cavitating flow, each square pixel can be fully or partially occupied by a vaporous phase, i.e. $0 \leq \alpha_G \leq 1$. In an Eulerian reference frame, the time difference of α_G can provide information on the local growth or collapse of the cavities. In this study, the first-order time difference of α_G field is defined as $\delta\alpha_G(x, y, t_{k-1}) = \alpha_G(x, y, t_k) - \alpha_G(x, y, t_{k-1})$, where the index k indicates the current instant. Therefore, $\delta\alpha_G > 0$ corresponds to local growth of the cavitation structure, and correspondingly $\delta\alpha_G < 0$ at a position in the flow field refers to the occurrence of a collapse. A value of $\delta\alpha_G = 0$ means that a similar fluid phase is present at the same location at the instants t_{k-1} and t_k; hence, it does not show any growth or collapse. Here, $\delta\alpha_G > 0$ and $\delta\alpha_G < 0$ are symbolized as $\delta\alpha_G{}^+$ and $\delta\alpha_G{}^-$, respectively. Appendix B illustrates the spatiotemporal variations of $\delta\alpha_G$, averaged in the y-direction at each instant, for only 5% of the total recording time of $T = 0.895$ s. The process of obtaining $\overline{\delta\alpha}_G(x, t)$ is commonly called the frame difference method (Sato, Taguchi & Hayashi 2013).

Visualization results given in § 4.4 reveal that PAM additives suppress cloud cavitation under moderate conditions and alleviate the growth of cavity fronts in the supercavitation regime. It is well understood that the propagation of high-speed pressure waves induced by the collapse of cavitation bubbles in a pure water flow intensifies the pressure fluctuations in the flow field and enhances the cavitation process (Karathanassis *et al.* 2018; Zhang *et al.* 2019; Wu *et al.* 2021). Therefore, it can be hypothesized that polymer additives reduce cavitation intensity by affecting the local collapse and growth process in the flow field. To verify this hypothesis, the r.m.s. of the fluctuations of the time difference fields, i.e. $(\delta\alpha)'_{G,rms}$, were calculated separately for the collapse and growth regions in each solution flow. The resultant r.m.s. fields were normalized by their associated time-averaged fields $\langle\delta\alpha_G\rangle$. It is assumed here that the cavitation process is statistically symmetric relative to the centreline $y = 0$ and shows the most intense fluctuations in the streamwise direction and on the centreline. Here, $(\delta\alpha)'_{G^-,rms}/\langle\delta\alpha_{G^-}\rangle$ is the defined to be the cavitation collapse level (CCL).

Figure 16(*a–d*) show the variation of the normalized time variance fluctuations of collapse on $y = 0$, respectively, for water and 100, 200 and 400 p.p.m. solution flows. The maxima of the profiles are highlighted by cyan circles and connected via dashed black lines to demonstrate the trend of changes. Figure 16(*a*) illustrates that increasing the water flow rate elevates the CCL. For the highest tested throat Reynolds number, $Re_{th} = 4.5 \times 10^4$, the collapse fluctuations can be as high as 10× the mean collapse time

https://doi.org/10.1017/jfm.2022.910 Published online by Cambridge University Press

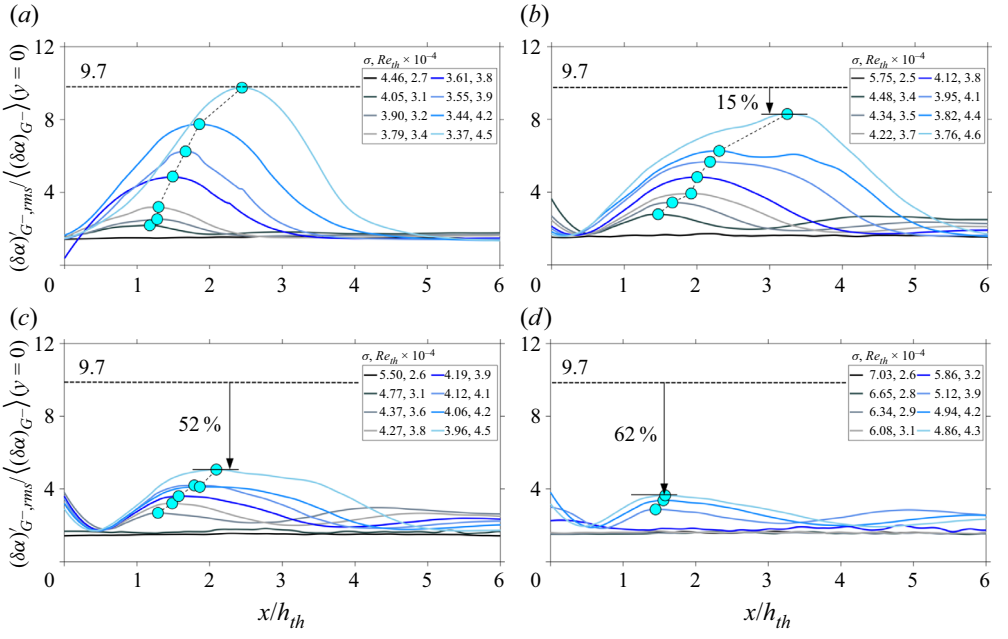

Figure 16. Streamwise variation of the normalized r.m.s. of the time difference fluctuations of the collapsing vapour ratio field on the centreline $y = 0$ for (*a*) pure water and (*b*) 100 p.p.m., (*c*) 200 p.p.m. and (*d*) 400 p.p.m. PAM solutions in water at different flow conditions. The maxima positions are highlighted by cyan circles and connected by a black dashed line on each figure to elucidate their variation. The reduction of the maximum CCL at the highest flow rate in each PAM solution relative to its counterpart in pure water is also annotated in each figure.

variance, revealing the extreme violence and chaos associated with the supercavitation regime. Until $Re_{th} = 3.4 \times 10^4$, pure water flow experiences the highest collapse level at $x \approx 1.2h_{th}$. With ≈10 % increase in the flow rate, the CCL shows a rapid increase, and the position of its peak shifts farther downstream to $x \approx 1.8h_{th}$. After $Re_{th} = 3.4 \times 10^4$, maximum CCL continues to elevate almost linearly with an increase in the flow rate.

Figure 16(*b*) shows that the cavitation process in the 100 p.p.m. solution occurs with relatively lower CCLs compared with the cavitating pure water flow, where the maximum CCL shifts downstream almost linearly for the entire range of the tested conditions. At the highest tested flow rate with $Re_{th} = 4.6 \times 10^4$, maximum CCL occurs at $x \approx 2.2h_{th}$ and $x \approx 3.1h_{th}$, respectively, for the pure water and the 100 p.p.m. solution flows, while the maximum CCL is relatively 15 % lower in the 100 p.p.m. solution. Also, compared with pure water, the PAM additives flatten the CCL profiles and relax the fluctuations globally. This result elucidates the CR effects of PAM additives. As figure 16(*c*,*d*) illustrate, a further increase of the solution concentration to 200 and 400 p.p.m. alleviates the fluctuations significantly. For the maximum flow rate tested, the cavitation collapse level reduces by 52 % and 62 % for the 200 and 400 p.p.m. solutions.

The dependency of the maximum values of CCL and cavitation growth level (CGL) on Re_{th} and σ are depicted in figure 17(*a*,*b*). Here, $(\delta\alpha)'_{G^+,rms}/\langle\delta\alpha_{G^+}\rangle$ is denoted as CGL. Statistically, the absolute values of CCL and CGL should be identical. In the current study, the maximum relative difference between the absolute CCL and CGL is ≈0.1 %. Figure 17(*a*) shows that the cavitation collapse and growth fluctuations increase by increasing Re_{th} for pure water. As discussed in § 4.4 and shown in figure 17(*a*), PAM

https://doi.org/10.1017/jfm.2022.910 Published online by Cambridge University Press

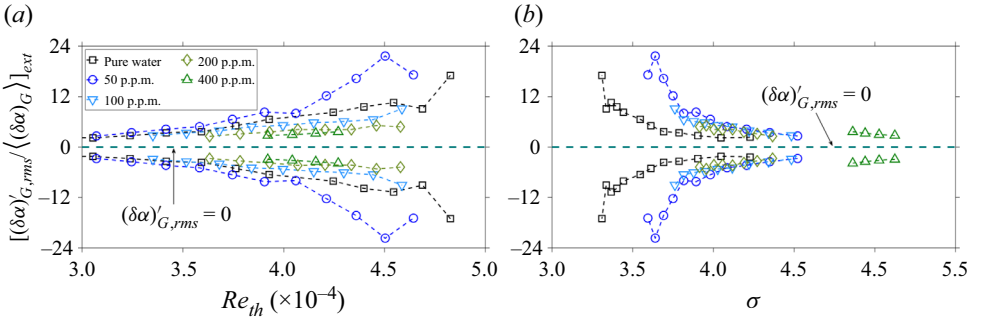

Figure 17. Variation of the extrema of the collapsing and growing $(\delta\alpha)'_{G,rms}$, normalized by its corresponding extrema of $\langle\delta\alpha_G\rangle$ versus (*a*) Re_{th} and (*b*) σ, for pure water and different solutions of PAM in water. The subscript 'ext' stands for extrema, i.e. a maximum or a minimum.

additives elevate the maximum CCL in the 50 p.p.m. solution relative to the pure water flow. This behaviour of the 50 p.p.m. solution escalates in the supercavitation regime. For solution concentrations more than 50 p.p.m., PAM additives reveal a CR effect by relaxing the maximum CCL and CGL in the entire range of the tested Re_{th}. As figure 17(*b*) shows, in a similar manner, a reduction in σ exacerbates the cavitation process by increasing CCL. This increase is abrupt for water and the 50 p.p.m. solution and relaxes for higher concentrations. As discussed in § 4.3, for a similar Re_{th}, the addition of PAM additives increases the pressure drop over the nozzle compared with pure water. Hence, CCL and CGL profiles do not collapse on the same abscissa in figure 17(*b*).

4.7. *Shedding frequency*

It was discussed in § 4.6 that one mechanism through which the PAM additives relax the cavitation process is by significantly mitigating the collapse and growth fluctuations in the flow field. Tracking the temporal evolution of the cavitation structures in the PAM solutions (see figure 13) reveals that additives also alter the shedding periodicity. A spectral analysis was performed on the high-speed pressure sensor data, explained in § 2.1, to quantify this behaviour. Two approaches were applied to the time series of the pressure fluctuations $p'_d(t)$ to obtain the spectra of the dominant shedding frequencies: (1) fast Fourier transform (FFT) was utilized to obtain the power spectral density (PSD) of the data, i.e. $\mathcal{A}_{PSD}(f)$, where f is the frequency; and (2) continuous wavelet transform (CWT) was used to obtain the time-dependent spectra of the shedding frequencies, i.e. $\mathcal{A}_{CWT}(f)$. The probability of the instantaneous dominant frequencies $\mathcal{A}_{pdf}(f)$ was obtained from the CWT results.

Figure 18(*a*,*b*) illustrate the spectral analysis results for two sample flow conditions with an intermediate and a high flow rate in pure water flow, and figure 18(*c*,*d*) show similar results for the 200 p.p.m. PAM solution. For each flow condition, left to right diagrams illustrate the temporal variation of the pressure fluctuations normalized by its maximum value, the PSD spectrum, the CWT spectrogram of the pressure signal, and the normalized probability density function (p.d.f.) percentage of the maximum CWT-based signal frequency. The maximum dominant frequencies obtained from the PSD-based and CWT-based spectral analysis were used to calculate the Strouhal number St, given in (3.2), for different solutions in the range of the tested flow conditions. Using the throat hydraulic diameter $D_{h,th}$ as the characteristic length scale in (3.2), the resultant $St(Re_{th})$

https://doi.org/10.1017/jfm.2022.910 Published online by Cambridge University Press

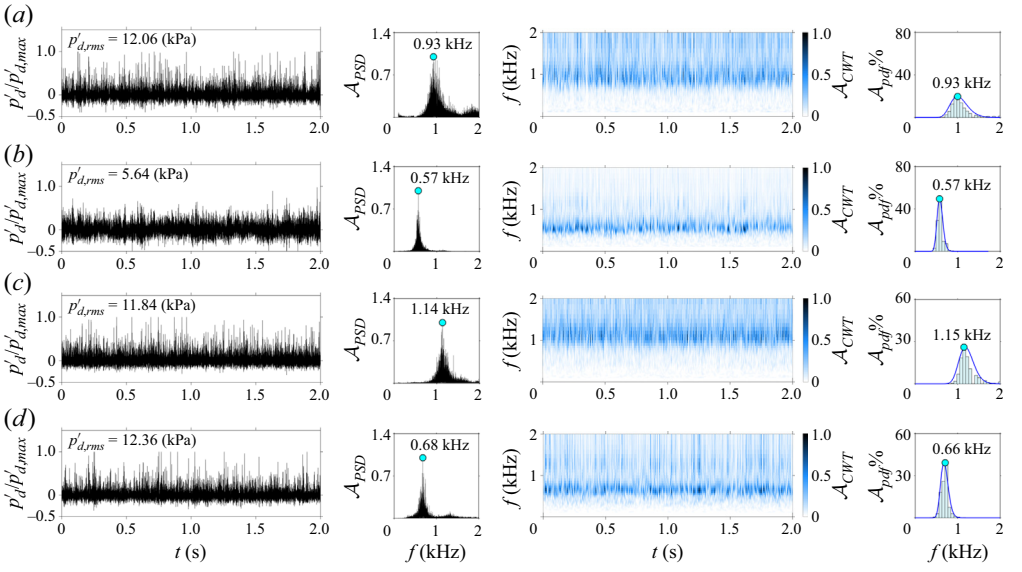

Figure 18. Spectral analysis results of the pressure fluctuation signal at the channel downstream, p'_d, in pure water flow at (*a*) $Re_{th} = 3.6 \times 10^4$, $\sigma = 3.69$ and (*b*) $Re_{th} = 4.8 \times 10^4$, $\sigma = 3.31$, and in 200 p.p.m. solution flow at (*c*) $Re_{th} = 3.6 \times 10^4$, $\sigma = 4.48$ and (*d*) $Re_{th} = 4.8 \times 10^4$, $\sigma = 4.86$. Cavitation onset of pure water and 200 p.p.m. solution occur, respectively, at $Re_{th,i} = 2.5 \times 10^4$, $\sigma_i = 4.71$ and $Re_{th,i} = 3.3 \times 10^4$, $\sigma_i = 4.42$. In each of (*a–d*) subplots from left to right represent, respectively, the pressure fluctuation signal at the channel's downstream, p'_d, normalized by its maximum value $p'_{d,max}$, for a period of 2 s; the normalized PSD of p'_d as a function of frequency, obtained using discrete FFT; the time-dependent behaviour of the signal's frequency, coloured by the normalized amplitude of the signal's CWT; and the normalized p.d.f. percentage of the maximum CWT-based signal frequency. Cyan circles on the PSD and p.d.f. plots highlight the maximum dominant frequencies obtained using FFT and CWT.

and $St(\sigma)$ profiles of different solutions are plotted, respectively, in figure 19(*a*,*b*). The first and second rows are associated with the PSD and CWT spectral analysis. Comparing the PSD-based and CWT-based results for $St(Re_{th})$ and $St(\sigma)$, the maximum relative difference was less than 1.5 % in the entire range of the tested solution concentrations and flow conditions. Therefore, the following discussion is attributed to both spectral analyses.

Figure 19(*a*) shows that St is almost constant before the cavitation onset in the pure water flow and is followed by a rapid increase in St as the flow begins to cavitate. After the onset, St reduces exponentially as the flow rate increases. The PAM solutions with concentrations in the range of 50–100 p.p.m. show a similar trend of changes in the $St(Re_{th})$ profile, with relatively smaller peaks of St. At a constant $Re_{th} > Re_{th,i}$, the 200 p.p.m. solution shows larger St relative to the pure water and other concentrations. In contrast, the 400 p.p.m. solution demonstrates lower St than the other semidilute solutions until its inception at $Re_{th,i} = 3.7 \times 10^4$, after which St suddenly increases to values relatively higher than the other tested solutions. As figure 19(*a*) illustrates, the dominant shedding frequency at the inception reduces by increasing the solution concentration. Figure 19(*b*) shows that the St of the pure water abruptly increases as the cavitation process starts and gradually decreases as σ decreases. The PAM solutions of 50 to 200 p.p.m. show similar trends of changes in $St(\sigma)$ profiles. As the flow rate increases and $\sigma \approx 6$ in the 400 p.p.m. solution, St increases slightly and maintains a value of $St \approx 0.1$ until the inception point, where St suddenly increases to $St \approx 0.2$, which is ≈70 % smaller than the inception St of

https://doi.org/10.1017/jfm.2022.910 Published online by Cambridge University Press

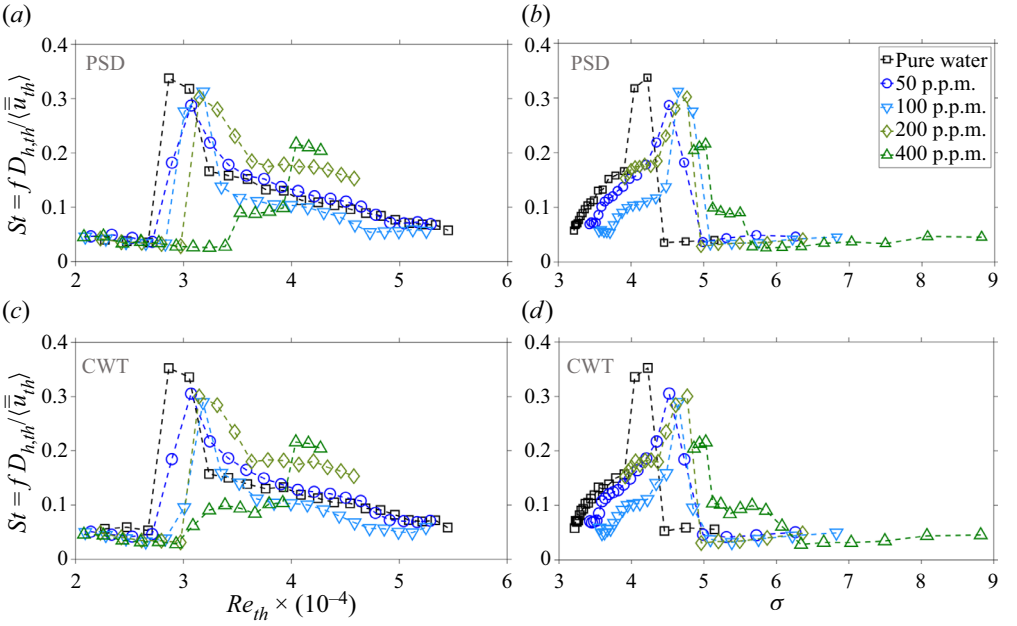

Figure 19. Throat hydraulic diameter $D_{h,th}$ based Strouhal number St (see (3.2)) as a function of (a) the throat Reynolds number Re_{th}, and (b) cavitation number σ in pure water and different PAM solution flows. Panels (a,b) and (c,d) display the results of PSD and CWT spectral analysis, respectively.

the pure water. These findings suggest that another mechanism by which the viscoelastic polymer molecules damp out cavitation is by reducing the dominant inception shedding frequency.

Strouhal numbers were also calculated based on the cavitation length L_{ca}. The resultant profiles are illustrated in figure 20(a,b). As shown in figure 20(a), the St profile of pure water flow shows a local peak at the cavitation onset and after a slight decrease starts to increase almost linearly, in contrast to its counterpart in figure 19(a). This highlights that as Re_{th} increases, the increase in L_{ca} dominates the decrease in f. The $St(Re_{th})$ profiles of 50 and 100 p.p.m. solutions in figure 20(a) show similar local peaks at the cavitation onset, with a reduced amplitude relative to the pure water. After the onset, St remains almost constant with an increase of Re_{th} for the 50 and 100 p.p.m. solutions. The St definition based on L_{ca} is ill-defined for non-cavitating flow. For instance, the 200 and 400 p.p.m. solutions have $L_{ca} = 0$ at $Re_{th} \lesssim 3.2 \times 10^4$, equivalent to $St = 0$ in this range. For higher Re_{th}, St grows linearly in both concentrations, with a smaller slope than that of pure water flow. As shown in figure 20(b), as σ decreases, $St(\sigma)$ profiles of the solutions display similar trends as of $St(Re_{th})$ for increasing Re_{th}.

5. Conclusion

An experimental study was conducted to elucidate the mechanisms of CR in viscoelastic semidilute polymer solutions. For this aim, a mesoscale converging–diverging nozzle with a throat size of 2 mm was designed. Temporal evolution and spatial variation of cavitation structures were captured using a high-speed imaging system. Instantaneous fluctuations of the downstream pressure were also recorded using high-frequency pressure sensors. A wide range of flow conditions, $2 \times 10^4 < Re_{th} < 5 \times 10^4$ and $3 < \sigma < 9$, was tested for

https://doi.org/10.1017/jfm.2022.910 Published online by Cambridge University Press

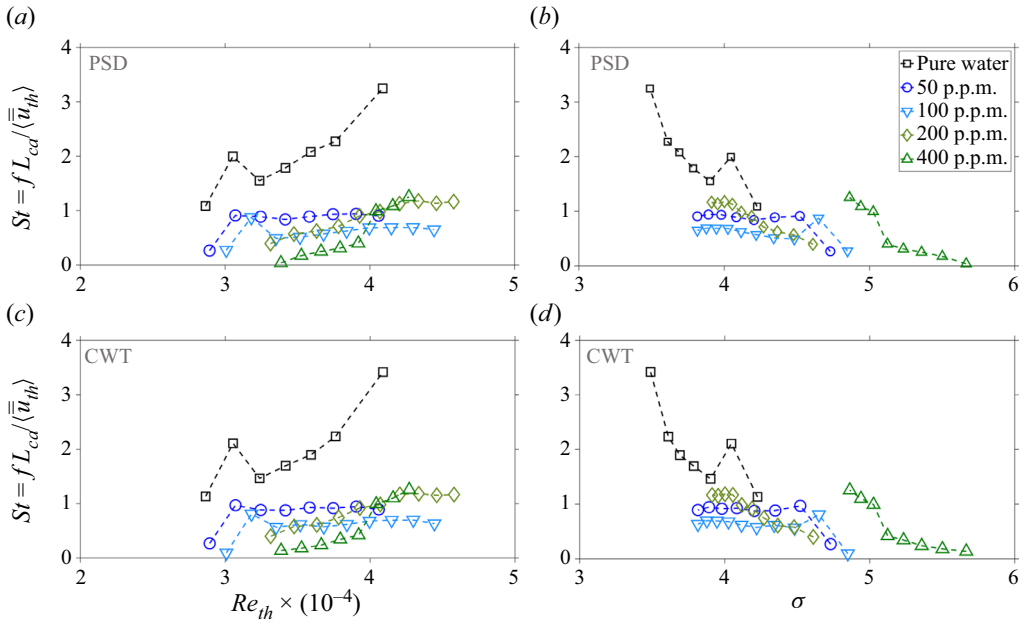

Figure 20. Cavitation length L_{ca} based Strouhal number St (see (3.2)) as a function of (*a*) the throat Reynolds number Re_{th}, and (*b*) cavitation number σ in pure water and different PAM solution flows. Panels (*a*,*b*) and (*c*,*d*) display the results of PSD and CWT spectral analysis.

pure water flow and PAM concentrations of 50–400 p.p.m. Rheological measurements suggested that concentrations less than 100 p.p.m. had constant viscosities in the range of the tested shear rates, with viscosities of 5 %–20 % more than the pure water. Solutions with $C_s \geq 200$ p.p.m. indicated shear-thinning behaviour with infinite shear viscosities relatively larger than the pure water flow. Numerical simulations showed that the wall shear stress at the throat could be as high as 1000 Pa, where the wall shear viscosity is too close to its infinite value. This result suggests that viscosity plays a minor role in the cavitation reduction mechanism of polymer additives. The PAM additives caused a $DR \approx 50\,\%$ for the maximum tested flow rate in the straight tube but increased the pressure drop over the nozzle relative to the pure water flow. Local increase of the shear viscosity at the nozzle inlet with relatively lower shear strain rates was the main reason for the pressure drop increase in PAM solutions

Visualization of the temporal evolution of vapour ratio fields on the channel's midspan reveals that the addition of PAM additives delays the cavitation onset to higher flow rates. Microcollapsing bubbles densely populate the edge of cloud cavitation in the pure water flow. In contrast, in PAM solutions, wall cavities grow in the form of streaky structures in the direction of the core liquid flow, with relatively smoother interfaces, where dispersed micron-sized collapsing bubbles are scarce. The mean cavitation length L_{ca}, which was determined based on the position of the peak of $\alpha'_{G,rms}$, increased almost linearly with the throat's Reynolds number Re_{th} and decreased linearly with the cavitation number σ in all the tested solutions. At a similar Re_{th}, PAM concentrations of 50 and 100 p.p.m. showed an increase in L_{ca} relative to the pure water flow. As the solution concentration increased to more than 100 p.p.m., cavitation growth started to attenuate. In the 400 p.p.m. solution, at $Re_{th} = 4 \times 10^4$, L_{ca} is reduced by 30 % relative to the pure water.

https://doi.org/10.1017/jfm.2022.910 Published online by Cambridge University Press

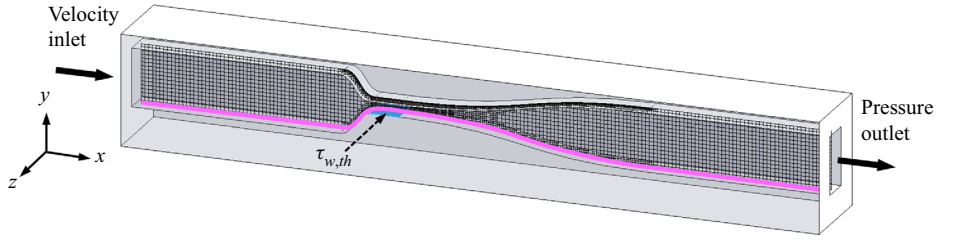

Figure 21. Representation of the channel geometry and the main boundary conditions used in the simulations. Mesh structure projected on the midspan of the channel is also illustrated. The pink sketch shows the wall profile at the midspan, and the region shadowed in blue displays the location of the lower throat wall, on which the streamwise shear stress was averaged, i.e. $\tau_{w,th}$.

Collapse and growth levels in cavitating water and solution flows were determined by calculating the fluctuations of the vapour-ratio time variance. The results indicated that the collapse and growth process of cavitation bubbles in pure water occurs at relatively higher levels as the flow rate and the pressure drop over the nozzle increase. The tested PAM solutions showed a similar trend of CCL and CGL increase by increasing the flow rate. For the entire range of tested flow conditions, the CCL of PAM solutions showed significant reductions relative to the pure water, with flattened variation profiles in the streamwise direction. As the PAM concentration increased in the solution, CCL reduced. The maximum level at which the cavitation bubbles collapse in the flow of the 400 p.p.m. solution is 60 % lower than the collapse level in the pure water at the highest tested Re_{th}. This result elucidates that the attenuation of the extreme collapse and growth fluctuations in a cavitating flow field is one of the main mechanisms by which polymer molecules reduce cavitation.

By spectral analysis of the measured downstream pressure fluctuations, it was found that the St of the pure water and the PAM solutions indicate a sudden peak at the cavitation inception and gradually reduces for higher Re_{th} and smaller σ. The inception St reduces significantly in the PAM solutions relative to the pure water. This reduction is $\approx$70 % in the 400 p.p.m. solution, which suggests that mitigation of the shedding frequency of the cavitating structures is another mechanism by which the PAM additives relax the cavitation process.

Supplementary movies. Supplementary movies are available at https://doi.org/10.1017/jfm.2022.910.

Acknowledgements. The authors gratefully acknowledge financial support from the Natural Sciences and Engineering Research Council (NSERC) of Canada.

Funding. This research received no specific grant from any funding agency, commercial or not-for-profit sectors.

Declaration of interests. The authors report no conflict of interest.

Author ORCIDs.
Reza Azadi https://orcid.org/0000-0003-1090-1518;
David S. Nobes https://orcid.org/0000-0002-9391-9563.

Appendix A. Numerical prediction of wall pressure

The Flow Simulation toolbox of a commercial software (SOLIDWORKS, 2021, Dassault Systems) was utilized as an ancillary tool in the design process of the nozzles and to

https://doi.org/10.1017/jfm.2022.910 Published online by Cambridge University Press

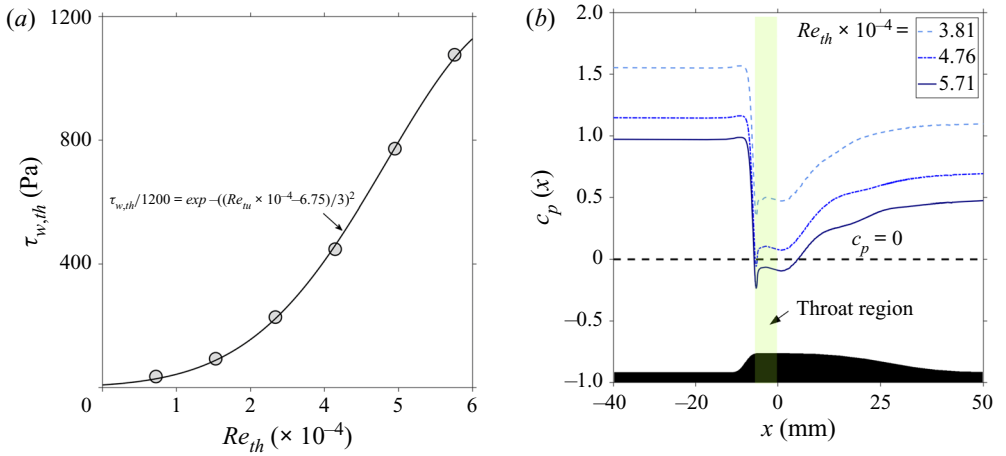

Figure 22. (*a*) Changes of the average streamwise throat wall shear stress, $\tau_{w,th}$ with the throat Reynolds number Re_{th}. Here, the grey circles show the simulation results, and the black profile is a Gaussian fit on the results, with its equation inserted into the figure. The fit's coefficient of determination is $R = 0.9993$. (*b*) Variation of the pressure coefficient c_p with the streamwise position x on the lower wall at the midspan of the channel. Line $c_p = 0$ is illustrated with a horizontal black dashed line on the plot. A pale-green rectangle highlights the throat region. The projection of the lower channel wall on the midspan plane is inserted below the diagram for reference. The black regions show the body of the test section.

estimate the position of the minimum pressure point in the channel. Water at 20 °C was used as the operating fluid. As given in figure 21, the average velocity was prescribed at the inlet, and the outlet of the flow domain was set at the atmospheric condition. The walls were assumed to be smooth, and the mesh was refined adjacent to the walls to resolve the boundary layer. The turbulence k–ϵ model was activated locally where the flow was fully turbulent. The flow domain was discretized using regular structured grids. A total of 3.5×10^6 mesh cells, with 2×10^6 cells in contact with the walls, were used for the simulations. This mesh configuration gave a solution independent of the grid size. A parametric study was conducted on the design for a range of $\theta_c = 24°$–$60°$ and $\theta_d = 6°$–$24°$, with steps of 12°, and $h_{th} = 1$–3 mm, with a step of 0.5 mm, and $\dot{V} = 2$–14 l min^{-1}, with a step of 2 l min^{-1}. It was found that the design with $\theta_c = 60°$, $\theta_d = 12°$ and $h_{th} = 2$ mm, was the optimum one considering the range of cavitation patterns of interest and the available experimental capabilities, such as the pump power.

Here, the pressure coefficient is defined as $c_p = p_w/0.5\rho u_{th}{}^2$. Figure 22(b) shows the variation of c_p in the streamwise direction, x, for three different Re_{th}. The plots were obtained by extracting pressure on the channel's lower wall, on the midspan plane, shown by a pink profile in figure 21. As the flow enters the convergence region, wall pressure drops sharply for all tested cases. Wall pressure has its minimum value at the throat entrance. For $Re_{th} > 4.76 \times 10^4$, wall pressure drops below the flow's saturation pressure, p_{sat}, and conditions are desirable for the cavitation to initiate. After a subtle increase, c_p is relatively constant through the throat region, after which it starts to recover smoothly to $c_p > 0$ in the divergence region. At a higher flow rate (here, $Re_{th} > 5.71 \times 10^4$), wall pressure stays well below p_{sat}, which increases the chances of a more violent cavitation process.

https://doi.org/10.1017/jfm.2022.910 Published online by Cambridge University Press

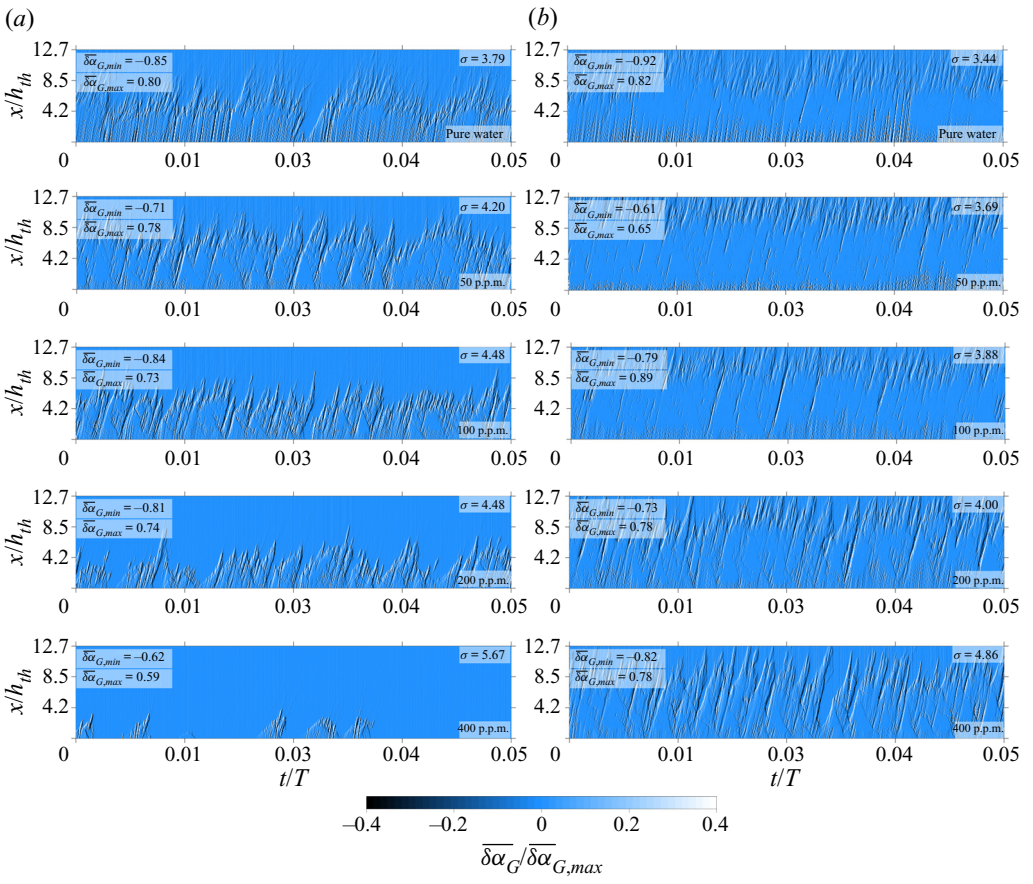

Figure 23. Spatiotemporal fields of y-averaged time difference of vapour ratio field $\overline{\delta\alpha}_G$, normalized by its maximum value, for (*a*) $Re_{th} = 3.4 \times 10^4$ and (*b*) $Re_{th} = 4.3 \times 10^4$. Each row corresponds to a different concentration, for which the value is annotated in the figure. Here, $T = 0.895$ s. The colour bar range is limited to ± 0.4 for better contrast.

Appendix B. Time variance fields of the cavitating flows

Figure 23(*a*,*b*) demonstrate the evolution of cavitation structures at two Re_{th} for pure water and four different PAM solutions, obtained using the frame difference method (Sato, Taguchi & Hayashi 2013).

References

Arndt, R.E.A. 2002 Cavitation in vortical flows. *Annu. Rev. Fluid Mech.* **34**, 143–175.

Arosemena, A.A., Andersson, H.I. & Solsvik, J. 2020 Turbulent channel flow of generalized Newtonian fluids at a low Reynolds number. *J. Fluid Mech.* **908**, A43.

Bird, R.B., Armstrong, R.C. & Hassager, O. 1987 *Dynamics of Polymeric Liquids. 1, 2nd edn: Fluid Mechanics*, pp. 171–175. John Wiley & Sons.

Brennen, C. 1970 Some cavitation experiments with dilute polymer solutions. *J. Fluid Mech.* **44** (1), 51–63.

Brennen, C.E. 2013 *Cavitation and Bubble Dynamics*, pp. 217–240. Cambridge University Press.

Brujan, E. 2011 *Cavitation in Non-Newtonian Fluids*, pp. 7–24. Springer.

Chahine, G.L., Kapahi, A., Choi, J.-K. & Hsiao, C.-T. 2016 Modeling of surface cleaning by cavitation bubble dynamics and collapse. *Ultrason. Sonochem.* **29**, 528–549.

https://doi.org/10.1017/jfm.2022.910 Published online by Cambridge University Press

CHATTERJEE, D. & ARAKERI, V.H. 1997 Towards the concept of hydrodynamic cavitation control. *J. Fluid Mech.* **332**, 377–394.

CURTISS, G.A., LEPPINEN, D.M., WANG, Q.X. & BLAKE, J.R. 2013 Ultrasonic cavitation near a tissue layer. *J. Fluid Mech.* **730**, 245–272.

DUBIEF, Y., WHITE, C.M., TERRAPON, V.E., SHAQFEH, E.S.G., MOIN, P. & LELE, S.K. 2004 On the coherent drag-reducing and turbulence-enhancing behaviour of polymers in wall flows. *J. Fluid Mech.* **514**, 271–280.

DULAR, M., BACHERT, B., STOFFEL, B. & ŠIROK, B. 2004 Relationship between cavitation structures and cavitation damage. *Wear* **257** (11), 1176–1184.

ESCUDIER, M.P., GOULDSON, I.W., PEREIRA, A.S., PINHO, F.T. & POOLE, R.J. 2001 On the reproducibility of the rheology of shear-thinning liquids. *J. Non-Newtonian Fluid Mech.* **97** (2–3), 99–124.

FRUMAN, D.H. 1999 Effects of non-Newtonian fluids on cavitation. In *Advances in the Flow and Rheology of Non-Newtonian Fluids* (ed. D.A. Siginer, D. De Kee & R.P. Chhabra), Rheology Series, vol. 8, pp. 209–254. Elsevier.

FUJIKAWA, S. & AKAMATSU, T. 1980 Effects of the non-equilibrium condensation of vapour on the pressure wave produced by the collapse of a bubble in a liquid. *J. Fluid Mech.* **97** (3), 481–512.

GANESH, H., MÄKIHARJU, S.A. & CECCIO, S.L. 2016 Bubbly shock propagation as a mechanism for sheet-to-cloud transition of partial cavities. *J. Fluid Mech.* **802**, 37–78.

HASEGAWA, T.T., USHIDA, A.A. & NARUMI, T. 2009 Huge reduction in pressure drop of water, glycerol/water mixture, and aqueous solution of polyethylene oxide in high speed flows through micro-orifices. *Phys. Fluids* **21** (5), 052002.

HOLMGREN, M. 2021 X Steam, Thermodynamic properties of water and steam. - File Exchange - MATLAB Central. https://www.mathworks.com/matlabcentral/fileexchange/9817-x-steam-thermodynamic-properties-of-water-and-steam.

HOYT, J.W. 1976 Effect of polymer additives on jet cavitation. *Trans. ASME J. Fluids Engng* **98** (1), 106–111.

INOUÉ, S. & SPRING, K.R. 1997 *Video Microscopy: The Fundamentals*, pp. 13–116. Plenum Press.

KARATHANASSIS, I.K., TRICKETT, K., KOUKOUVINIS, P., WANG, J., BARBOUR, R. & GAVAISES, M. 2018 Illustrating the effect of viscoelastic additives on cavitation and turbulence with X-ray imaging. *Sci. Rep.* **8** (1), 14968.

KAWANAMI, Y., KATO, H., YAMAGUCHI, H., TANIMURA, M. & TAGAYA, Y. 1997 Mechanism and control of cloud cavitation. *J. Fluids Engng* **119** (4), 788–794.

LUMLEY, J.L. 1973 Drag reduction in turbulent flow by polymer additives. *J. Polym. Sci.* **7** (1), 263–290.

MANE, M.B., BHANDARI, V.M., BALAPURE, K. & RANADE, V.V. 2020 Destroying antimicrobial resistant bacteria (AMR) and difficult, opportunistic pathogen using cavitation and natural oils/plant extract. *Ultrason. Sonochem.* **69**, 105272.

MIN, T., YOO, J.Y., CHOI, H. & JOSEPH, D.D. 2003 Drag reduction by polymer additives in a turbulent channel flow. *J. Fluid Mech.* **486**, 213–238.

MORRISON, F.A. 1998 *Understandig Rheology*, pp. 382–437. Oxford University Press.

MURAKAMI, K., YAMAKAWA, Y., ZHAO, J., JOHNSEN, E. & ANDO, K. 2021 Ultrasound-induced nonlinear oscillations of a spherical bubble in a gelatin gel. *J. Fluid Mech.* **924**, A38.

NASERI, H., KOUKOUVINIS, P., MALGARINOS, I. & GAVAISES, M. 2018 On viscoelastic cavitating flows: a numerical study. *Phys. Fluids* **30** (3), 033102.

ŌBA, R., ITŌ, Y. & URANISHI, K. 1978 Effect of polymer additives on cavitation development and noise in water flow through an orifice. *Trans. ASME J. Fluids Engng* **100** (4), 493–499.

OWOLABI, B.E., DENNIS, D.J.C. & POOLE, R.J. 2017 Turbulent drag reduction by polymer additives in parallel-shear flows. *J. Fluid Mech.* **827**, R4.

PTASINSKI, P.K., BOERSMA, B.J., NIEUWSTADT, F.T.M., HULSEN, M.A., VAN DEN BRULE, H.A.A. & HUNT, J.C.R. 2003 Turbulent channel flow near maximum drag reduction: simulations, experiments and mechanisms. *J. Fluid Mech.* **490** (490), 251–291.

ROOD, E.P. 1991 Review, mechanisms of cavitation inception. *Trans. ASME J. Fluids Engng* **113** (2), 163–175.

SATO, K., TAGUCHI, Y. & HAYASHI, S. 2013 High speed observation of periodic cavity behavior in a convergent-divergent nozzle for cavitating water jet. *J. Flow Control Meas. Visual.* **1** (3), 102–107.

STRIDE, E. & COUSSIOS, C. 2019 Nucleation, mapping and control of cavitation for drug delivery. *Nat. Rev. Phys* **1**, 495–509.

STRIDE, E., SEGERS, T., LAJOINIE, G., CHERKAOUI, S., BETTINGER, T., VERSLUIS, M. & BORDEN, M. 2020 Microbubble agents: new directions. *Ultrasound Med. Biol.* **46** (6), 1326–1343.

SYED MUSTAPHA, S.M.F.D., PHILLIPS, T.N., PRICE, C.J., MOSELEY, L.G. & JONES, T.E.R. 1999 Viscometric flow interpretation using qualitative and quantitative techniques. *Engng Appl. Artif. Intell.* **12** (3), 255–272.

https://doi.org/10.1017/jfm.2022.910 Published online by Cambridge University Press

TABOR, M. & DE GENNES, P.G. 1986 A cascade theory of drag reduction. *Europhys. Lett.* **2** (7), 519–522.
TING, R.Y. 1978 Characteristics of flow cavitation in dilute solutions of polyethylene oxide and polyacrylamide. *Phys. Fluids* **21** (6), 898–901.
TOMS, B.A. 1948 Some observations on the flow of linear polymer solutions through straight tubes at large Reynolds numbers. In *Proceedings of the 1st International Congress on Rheology*, vol. 2, pp. 135–141.
DEN TOONDER, J.M.J., DRAAD, A.A., KUIKEN, G.D.C. & NIEUWSTADT, F.T.M. 1995 Degradation effects of dilute polymer solutions on turbulent drag reduction in pipe flows. *Appl. Sci. Res.* **55** (1), 63–82.
TURNER, P., HODNETT, M., DOREY, R. & CAREY, J.D. 2019 Controlled sonication as a route to in-situ graphene flake size control. *Sci. Rep.* **9** (1), 8710.
VERHAAGEN, B. & FERNÁNDEZ RIVAS, D. 2016 Measuring cavitation and its cleaning effect. *Ultrason. Sonochem.* **29**, 619–628.
VERSLUIS, M., STRIDE, E., LAJOINIE, G., DOLLET, B. & SEGERS, T. 2020 Ultrasound contrast agent modeling: a review. *Ultrasound Med. Biol.* **46** (9), 2117–2144.
VIRK, P.S. 1975 Drag reduction fundamentals. *AIChE J.* **21** (4), 625–656.
VIRK, P.S., MICKLEY, H.S. & SMITH, K.A. 1970 The ultimate asymptote and mean flow structure in Toms' phenomenon. *Trans. ASME J. Appl. Mech.* **37** (2), 488–493.
WARWARUK, L. & GHAEMI, S. 2021 A direct comparison of turbulence in drag-reduced flows of polymers and surfactants. *J. Fluid Mech.* **917**, A7.
WHITE, C.M. & MUNGAL, M.G. 2008 Mechanics and prediction of turbulent drag reduction with polymer additives. *Annu. Rev. Fluid Mech.* **40** (1), 235–256.
WHITE, F.M. 2011 *Fluid Mechanics*, 7th edn. McGraw Hill.
WU, J., DEIJLEN, L., BHATT, A., GANESH, H. & CECCIO, S.L. 2021 Cavitation dynamics and vortex shedding in the wake of a bluff body. *J. Fluid Mech.* **917**, A26.
XI, L. 2019 Turbulent drag reduction by polymer additives: fundamentals and recent advances. *Phys. Fluids* **31** (12), 121302.
XU, S., WANG, J., CHENG, H., JI, B. & LONG, X. 2020 Experimental study of the cavitation noise and vibration induced by the choked flow in a Venturi reactor. *Ultrason. Sonochem.* **67**, 105183.
YASUDA, K., ARMSTRONG, R.C. & COHEN, R.E. 1981 Shear flow properties of concentrated solutions of linear and star branched polystyrenes. *Rheol. Acta* **20** (2), 163–178.
ZENG, Q., GONZALEZ-AVILA, S.R. & OHL, C.-D.D. 2020 Splitting and jetting of cavitation bubbles in thin gaps. *J. Fluid Mech.* **896**, A28.
ZHANG, H., ZUO, Z., MORCH, K.A. & LIU, S. 2019 Thermodynamic effects on Venturi cavitation characteristics. *Phys. Fluids* **31** (9), 097107.
ZUPANC, M., PANDUR, Ž., STEPIŠNIK PERDIH, T., STOPAR, D., PETKOVŠEK, M. & DULAR, M. 2019 Effects of cavitation on different microorganisms: the current understanding of the mechanisms taking place behind the phenomenon. A review and proposals for further research. *Ultrason. Sonochem.* **57**, 147–165.

https://doi.org/10.1017/jfm.2022.910 Published online by Cambridge University Press